

A direct measure of free electron gas via the kinematic Sunyaev-Zel’dovich effect in Fourier-space analysis

Naonori S. Sugiyama^{1,2*}, Teppei Okumura^{3,1} and David N. Spergel^{4,5}

¹ *Kavli Institute for the Physics and Mathematics of the Universe (WPI),*

Todai Institutes for Advanced Study, The University of Tokyo, Chiba 277-8582, Japan

² *CREST, Japan Science and Technology Agency, Kawaguchi, Saitama, Japan*

³ *Institute of Astronomy and Astrophysics, Academia Sinica, P. O. Box 23-141, Taipei 10617, Taiwan*

⁴ *Department of Astrophysical Sciences, Princeton University, Peyton Hall, Princeton NJ 08544-0010, USA*

⁵ *Center for Computational Astrophysics, Flatiron Institute, NY NY 10010, USA*

ABSTRACT

We present the measurement of the kinematic Sunyaev-Zel’dovich (kSZ) effect in Fourier space, rather than in real space. We measure the density-weighted pairwise kSZ power spectrum, the first use of this promising approach, by cross-correlating a cleaned cosmic microwave background (CMB) temperature map, which jointly uses both *Planck* Release 2 and *Wilkinson Microwave Anisotropy Probe* nine-year data, with the two galaxy samples, CMASS and LOWZ, derived from the Baryon Oscillation Spectroscopic Survey (BOSS) Data Release 12. To estimate the CMB temperature distortion associated with each galaxy, we apply an aperture photometry filter. With the current data, we constrain the average optical depth τ multiplied by the ratio of the Hubble parameter at redshift z and the present day, $E = H/H_0$; we find $\tau E = (3.95 \pm 1.62) \times 10^{-5}$ for LOWZ, which corresponds to the statistical significance of $S/N = 2.44$, and $\tau E = (1.25 \pm 1.06) \times 10^{-5}$ for CMASS, which is consistent with a null hypothesis of no signal. While this analysis results in the kSZ signals with only evidence for a detection, the combination of future CMB and spectroscopic galaxy surveys should enable precision measurements. We estimate that the combination of CMB-S4 and data from Dark Energy Spectroscopic Instrument should yield detections of the kSZ signal with $S/N = 70 - 100$, depending on the resolution of CMB-S4.

Key words: cosmology: cosmic background radiation – cosmology: large-scale structure of Universe – cosmology: observations – cosmology: theory – galaxies: intergalactic medium

1 INTRODUCTION

Sunyaev & Zeldovich (1970) showed that a cloud of moving free electrons induces brightness temperature anisotropies in the cosmic microwave background (CMB) radiation: the amplitude of the *kinematic* Sunyaev-Zel’dovich (hereafter, kSZ) is proportional to the product of the electron column density and the electron velocity. The kSZ signal thus offers a unique and powerful observational tool for a direct measurement of baryonic matter that is insensitive to the free electron gas temperature. The kSZ effect directly probes the difficult to detect ionized warm and hot intracluster medium and the intergalactic medium that is believed to contain most of the universe’s baryons (see e.g. Fukugita & Peebles (2004)). Because the signal is sensitive to the peculiar velocity probe, it

is potentially a powerful probe of large-scale velocity fields and cosmological parameters.

Based on the *pairwise* kSZ estimator proposed by Ferreira et al. (1999), Hand et al. (2012) reported the first clear detection of the kSZ effect using CMB data from the Atacama Cosmology Telescope (ACT; Swetz et al. (2011)) with galaxy positions from the Baryon Oscillation Spectroscopic Survey (BOSS; Eisenstein et al. (2011)), four decades after the theory of the effect was first proposed. Since this first detection several other detections have followed from multiple CMB experiments, cross-correlating with other galaxy or cluster catalogues: the Planck collaboration (Planck Collaboration et al. 2016a) used galaxy positions from the Sloan Digital Sky Survey Data Release 7 (SDSS-DR7; Abazajian et al. (2009)), the South Pole Telescope (SPT; George et al. (2015)) collaboration (Soergel et al. 2016) used cluster positions from the Dark Energy Survey

* E-mail: nao.s.sugiyama@gmail.com

(DES; The Dark Energy Survey Collaboration (2005); Dark Energy Survey Collaboration et al. (2016)), and De Bernardis et al. (2016) used CMB data from ACT with galaxy positions from BOSS. In addition to these kSZ measurements, Schaan et al. (2016) reported a detection of the kSZ signal by stacking the CMB temperature at the location of each halo, weighted by the corresponding reconstructed velocity, using CMB data from ACTPol (Naess et al. 2014) with galaxy positions from BOSS. Hill et al. (2016) and Ferraro et al. (2016) detected the kSZ effect through a three point correlation using CMB data from Planck and Wilkinson Microwave Anisotropy Probe (WMAP; Bennett et al. (2013)) with galaxy positions from the Wide-field Infrared Survey Explorer (WISE; Wright et al. (2010)).

The kSZ effect is well-suited for studying properties of the optical depth, τ , of haloes hosting galaxies or galaxy clusters. As the measured optical depth via the kSZ effect is insensitive to gas temperature and redshift, the kSZ effect can be used to detect ionized gas that is difficult to observe through its emission, so-called “missing baryons” (e.g., Fukugita et al. (1998); Fukugita & Peebles (2004); Bregman (2007)). Most of the missing baryons are thought to reside in a tenuous warm-hot intergalactic medium (WHIM) within a temperature range of $10^5 \text{ K} < T < 10^7 \text{ K}$ (Cen & Ostriker 1999; Davé et al. 1999; Cen & Ostriker 2006), which are neither hot enough ($T < 10^8 \text{ K}$) to be seen in X-ray observations, nor cold enough ($T > 10^3 \text{ K}$) to be made into stars and galaxies. Constraining the optical depth will allow one to investigate astrophysical effects such as star formation and feedback from active galactic nuclei and supernovae for a wide mass and redshift range of the haloes sourcing the kSZ signal (DeDeo et al. 2005; Bregman 2007; Hernández-Monteagudo & Sunyaev 2008; Ho et al. 2009; Hernández-Monteagudo & Ho 2009; Shao et al. 2011; Hernández-Monteagudo et al. 2015; Schaan et al. 2016; Flender et al. 2016b; Battaglia 2016; Flender et al. 2016a).

From a cosmological perspective, the kSZ effect is a potential proxy for the peculiar velocity of galaxies or galaxy clusters. The pairwise kSZ signal enables us to measure the *pairwise velocity* (Peebles 1980) at cosmological distances. This large-scale velocity information provides constraints on cosmological parameters, especially on the equation of state of dark energy and modified gravity models (DeDeo et al. 2005; Hernández-Monteagudo et al. 2006; Bhattacharya & Kosowsky 2007, 2008; Kosowsky & Bhattacharya 2009; Keisler & Schmidt 2013; Ma & Zhao 2014; Mueller et al. 2015b; Alonso et al. 2016; Sugiyama et al. 2016a) as well as the sum of the neutrino masses (Mueller et al. 2015a).

In Sugiyama et al. (2016a), we proposed a new statistic of the kSZ signal, the density-weighted pairwise kSZ power spectrum in Fourier space, while many previous works focused on the pair-weighted pairwise kSZ signal in configuration space. There, we showed that two effects, redshift space distortions (RSD) (Kaiser 1987) and the Alcock-Paczynski test (Alcock & Paczynski 1979), leave their distinctive features on the pairwise kSZ power spectrum, allowing us to infer cosmology from the joint analysis of the density and kSZ power spectra independent of our knowledge of the optical depth in a given tracer sample.

This work reports the first measurement of the pairwise kSZ power spectrum using a cleaned CMB map (Bobin et al.

2016), which jointly uses both Planck and WMAP data, with two samples of BOSS galaxies, LOWZ and CMASS, drawn from the final Data Release 12 (DR12; Alam et al. (2015)). We improve on previous, similar analyses in a number of ways. First, we use a theoretical model for the pairwise kSZ power spectrum including the RSD effect, which is developed in Sugiyama et al. (2016a). Secondly, we measure the “density-weighted” pairwise kSZ estimator normalized by a random catalogue, while almost all previous works measure the “pair-weighted” pairwise kSZ estimator normalized by an observed catalogue itself (Hand et al. 2012; Planck Collaboration et al. 2016a; Soergel et al. 2016; De Bernardis et al. 2016). This approach allows us to perform the analysis in Fourier space, namely measure the pairwise kSZ power spectrum, similarly to the galaxy power spectrum in clustering analysis. Thirdly, we use a random catalogue to both define number density fluctuations of galaxies and measure survey window functions, correcting for survey geometry effects. Fourth, to break a strong degeneracy among the optical depth τ , the linear logarithmic growth rate f , and the linear bias b in the pairwise kSZ signal, we fix the values of f and b , where they are measured from the RSD analysis of galaxy clustering (Gil-Marín et al. 2016) using the same galaxy samples as we use in this work. In this way, we do not constrain the optical depth τ itself but the product τE , where $E = H/H_0$, and H and H_0 are the Hubble parameter at given redshift and the present day, respectively. Finally, we repeat the pairwise kSZ power analysis for various angular radii of an aperture photometry filter, where the filter is used to estimate the CMB temperature distortion associated with each galaxy. We measure the optical depth τE as a function of aperture radii through this analysis and constrain parameters in an assumed gas profile as well as the gas-mass fraction via the measurement.

We provide a forecast of future kSZ measurements and their power to constrain optical depth models with an error model for the optical depth. We assume a hypothetical Stage-IV CMB experiment (CMB-S4; Abazajian et al. (2015)) with one current galaxy survey, BOSS, and two upcoming spectroscopic galaxy surveys, the Dark Energy Spectroscopic Instrument (DESI; Levi et al. (2013)) and the Subaru Prime Focus Spectrograph (PFS; Takada et al. (2014)).

This paper is organized as follows. In Section 2, we summarize the CMB and galaxy sample data used in our analysis. In Section 3, we describe our models for both the optical depth and the pairwise kSZ power spectrum. In Section 4, we explain the technique to measure the pairwise kSZ power spectrum, followed by the treatment of the survey window function in Section 5. Section 6 presents the method to estimate the covariance matrix of the pairwise kSZ power spectrum from data itself. In Section 7, the results including the best-fitting parameters of the filtered optical depth are presented. We give an overview of future kSZ measurements in Section 8. We present a summary and conclusions in Section 9. We additionally provide Appendix A that compute the pairwise kSZ power covariance in linear theory and compare it with the covariance estimates from data itself, Appendix B that details how to measure the pairwise kSZ power spectrum and Appendix C that gives detailed derivations of equations used in our analysis.

Throughout this paper we adopt a flat Λ CDM cosmology (Planck Collaboration et al. 2016c): $\Omega_m = 0.309$,

$\Omega_\Lambda = 0.691$, $n_s = 0.9608$, $\sigma_8 = 0.815$, and $H_0 = 100 h \text{ km s}^{-1} \text{ Mpc}^{-1}$ with $h = 0.68$. We use the best-fitting values of $f\sigma_8$ and $b\sigma_8$ measured in (Gil-Marín et al. 2016): $(f\sigma_8, b\sigma_8) = (0.392, 1.283)$ for LOWZ and $(0.445, 1.218)$ for CMASS.

2 DATA

2.1 WMAP and Planck maps

We use a cleaned CMB temperature map constructed from a novel component separation technique, “local-generalized morphological component analysis” (LGMCA; Bobin et al. (2013, 2014)) that uses both *Planck* Release 2 (PR2; Planck Collaboration et al. (2016b)) and *Wilkinson Microwave Anisotropy Probe* nine-year (*WMAP9*; Bennett et al. (2013)) data, where the PR2 and *WMAP9* maps contain nine and five channels, respectively. This WPR2 map is provided in *HEALPix* (Górski et al. 2005) pixelization scheme at a resolution of the grid expressed by $N_{\text{side}} = 2048$.

The WPR2 map is well suited for an analysis of the kSZ signal, as it is designed to have minimal galactic contamination and very little residual thermal Sunyaev-Zel’dovich (tSZ) signal. In this map, residual contamination of the tSZ is about 10^6 times smaller than the kSZ signal at any scale (see fig. 12 in Bobin et al. (2014)). We also use the WPR2 noise map made by applying the LGMCA technique to the Planck and WMAP noise maps, in order to perform a null test of the kSZ signal as a test of systematics (see Section 7).

2.2 BOSS galaxy catalogues

As proxies for haloes, we use two galaxy samples, the LOWZ sample with 463044 galaxies between $z = 0.15$ - 0.43 ($z_{\text{eff}} = 0.33$), and the CMASS sample with 849637 galaxies between $z = 0.43$ - 0.7 ($z_{\text{eff}} = 0.56$). These samples are drawn from the Baryon Oscillation Spectroscopic Survey (BOSS; Eisenstein et al. (2011); Bolton et al. (2012); Dawson et al. (2013)) Data Release 12 (DR12; Alam et al. (2015)) and are selected from multi-colour SDSS imaging (Fukugita et al. 1996; Gunn et al. 1998; Smith et al. 2002; Gunn et al. 2006; Doi et al. 2010). We also use the associated random catalogues that quantify the survey geometry of BOSS.

The LOWZ galaxies lie in massive haloes with mean halo masses of $5.2 \times 10^{13} h^{-1} M_\odot$, large-scale bias of ~ 2.0 and the satellite fraction of 12%, while the CMASS galaxies lie in halos with the masses of $2.6 \times 10^{13} h^{-1} M_\odot$, the bias ~ 2.0 and the satellite fractions 10% (White et al. 2011; Parejko et al. 2013; Bundy et al. 2015; Leauthaud et al. 2016; Saito et al. 2016). In our analysis, we use the CMASS and LOWZ galaxy samples in both the North Galactic Cap (NGC) and the South Galactic Cap (SGC).

To correct for several observational artefacts in the catalogues and obtain unbiased estimates of galaxy density fields, we use the following weight for each galaxy i (Ross et al. 2012; Anderson et al. 2014; Reid et al. 2016),

$$w_{c,i} = w_{\text{sys},i} (w_{\text{cp},i} + w_{\text{noz},i} - 1), \quad (1)$$

where w_{cp} , w_{noz} , and w_{sys} denote a redshift failure weight,

a collision weight, and an angular systematics weight, respectively. The details about the observational systematic weights are described in Reid et al. (2016). We do not apply the optimal weighting of galaxies, the so-called FKP weight (Feldman et al. 1994), because this weight is derived for the galaxy power spectrum and would be non-optimal for the pairwise kSZ spectrum.

3 THEORY

3.1 Kinematic Sunyaev-Zel’dovich effect

The scattering of CMB photons with electrons moving with respect to the rest frame of CMB, where the CMB is observed to be isotropic, causes anisotropies of the CMB brightness temperature. This bulk motion-induced thermal distortion is known as the kSZ effect. In the non-relativistic limit, the temperature anisotropies due to the kSZ effect is given by (Sunyaev & Zeldovich 1970, 1972, 1980; Ostriker & Vishniac 1986)

$$\delta T_{\text{kSZ}}(\hat{n}) = -T_0 \sigma_T \int dl \left(\frac{\vec{v}_e(\vec{x}) \cdot \hat{n}}{c} \right) n_e(\vec{x}), \quad (2)$$

where $T_0 = 2.725 \text{ K}$ is the average CMB temperature, n_e is the physical free electron number density, \vec{v}_e denotes the peculiar velocity of free electrons, σ_T is the Thomson scattering cross-section, and c is the speed of light. In this expression, the integral $\int dl$ is performed along the line-of-sight (LOS) given by \hat{n} . The sign of velocities is defined so that $\vec{v} \cdot \hat{n} > 0$ corresponds to a cloud of free electrons moving away from the observer. In this definition, the kSZ effect slightly shifts CMB temperature, lower (higher) for positive (negative) peculiar velocities, with preserving the CMB blackbody spectrum and without depending on free electron temperature.

3.1.1 Galaxies as point sources

We start with the simplifying assumption that observed galaxies sit the centres of their host haloes and can be treated as point sources. Under this assumption, we can describe the electron number density as

$$n_e(\vec{x}) = \frac{1}{a^3} \sum_i^N N_{e,i} \delta_D(\vec{x} - \vec{x}_i), \quad (3)$$

where $N_{e,i}$ means the total number of free electrons associated with galaxy i , N is the total number of observed galaxies, a is the scale factor, \vec{x}_i represents the three-dimensional coordinates of the galaxy, and δ_D is the Delta function. Then, equation. (2) becomes

$$\delta T_{\text{kSZ}}(\hat{n}) = - \sum_i^N \left(\frac{\vec{v}_{e,i} \cdot \hat{n}_i}{c} \right) \frac{T_0 \sigma_T N_{e,i}}{D_{A,i}^2} \delta_D(\hat{n} - \hat{n}_i), \quad (4)$$

where we used $\delta_D(\vec{x} - \vec{x}_i) = (1/\chi^2) \delta_D(\chi - \chi_i) \delta_D(\hat{n} - \hat{n}_i)$ and $\int dl = a \int d\chi$ with χ being the radial comoving distance, the free electron peculiar velocity $\vec{v}_{e,i}$ is evaluated at galaxy i , the line-of-sight (LOS) direction \hat{n}_i points to the galaxy from the observer, and $D_{A,i} = a\chi_i$ represents the angular diameter distance to the galaxy. In subsection 3.1.2, we will discuss the more realistic case where galaxies are not point sources but have gas profiles.

The observed kSZ temperature $\delta T_{\text{kSZ}}^{(\text{obs})}$ can be expressed as the convolution of the true kSZ temperature δT_{kSZ} with the instrumental beam function $B(\hat{n}, \hat{n}')$,

$$\delta T_{\text{kSZ}}^{(\text{obs})}(\hat{n}) = \int d\Omega_{\hat{n}'} B(\hat{n}, \hat{n}') \delta T_{\text{kSZ}}(\hat{n}'). \quad (5)$$

We approximate the Planck beam as a Gaussian,

$$\delta T_{\text{kSZ}}^{(\text{obs})}(\hat{n}) = - \sum_i^N \left(\frac{\vec{v}_{e,i} \cdot \hat{n}_i}{c} \right) \frac{T_0 \sigma_{\text{T}} N_{e,i}}{2\pi D_{A,i}^2 \sigma_{\text{B}}^2} e^{-(\hat{n} - \hat{n}_i)^2 / (2\sigma_{\text{B}}^2)}, \quad (6)$$

where σ_{B} is related to the effective beam full-width at half-maximum (FWHM) as $\sigma_{\text{B}} = \text{FWHM} / (\sqrt{8 \ln(2)}) = 0.4247 \text{ FWHM}$. In our analysis, we use $\text{FWHM} = 5'$ for the WPR2 map (Section. 2.1).

We apply an aperture photometry (AP) filter to estimate the CMB temperature distortion associated with each galaxy

$$\delta T_{\text{kSZ}}^{(\text{AP})}(\vec{\theta}) = \int d^2\theta' U(\vec{\theta} - \vec{\theta}') \delta T_{\text{kSZ}}^{(\text{obs})}(\vec{\theta}'), \quad (7)$$

where we describe the three-dimensional LOS unit vector \hat{n} as the two-dimensional vector $\vec{\theta}$ in the $\theta_x - \theta_y$ plane and centre each galaxy at the origin. The weight function $U(\vec{\theta})$ satisfies the criterion

$$\int_0^{\theta_c} d\theta \theta U(\theta) = 0, \quad (8)$$

where $\theta = |\vec{\theta}|$, and θ_c is the AP filter radius. In other words, $U(\theta)$ is taken to be a *compensated* radial weight function across the aperture. This filter is insensitive to CMB fluctuations on scales larger than the aperture radius, so that the contamination of primary CMB anisotropies to the kSZ signal in the filtered map is nearly uncorrelated on large scales (see Appendix A). Using the convolution theorem, equation (7) becomes

$$\delta T_{\text{kSZ}}^{(\text{AP})}(\vec{\theta}) = \int \frac{d^2\ell}{(2\pi)^2} e^{i\vec{\ell} \cdot \vec{\theta}} U(\ell\theta_c) \delta T_{\text{kSZ}}(\vec{\ell}) B(\vec{\ell}), \quad (9)$$

where $\vec{\ell}$ is the two-dimensional wavevector perpendicular to the LOS, $\ell = |\vec{\ell}|$, and $\delta T_{\text{kSZ}}(\vec{\ell})$ and $B(\vec{\ell})$ are the two-dimensional Fourier transforms of the kSZ temperature and the beam function, respectively. From equation (4), $\delta T_{\text{kSZ}}(\vec{\ell})$ is given by

$$\delta T_{\text{kSZ}}(\vec{\ell}) = - \sum_i^N \left(\frac{\vec{v}_{e,i} \cdot \hat{n}_i}{c} \right) \frac{T_0 \sigma_{\text{T}} N_{e,i}}{D_{A,i}^2} e^{-i\vec{\ell} \cdot \vec{\theta}_i}. \quad (10)$$

For a compensated top-hat window, we average the mean temperature within a disk of radius θ_c , and then subtract from it the mean temperature in a surrounding ring of inner and outer radii, where the outer radius is chosen to be $\sqrt{2}\theta_c$ so that the disk and ring have the same area (Planck Collaboration et al. 2016a; Schaun et al. 2016; De Bernardis et al. 2016). Then, the Fourier transform of the AP filter is given by (Alonso et al. 2016)

$$U(x) = 2 \left[W_{\text{top}}(x) - W_{\text{top}}(\sqrt{2}x) \right] \quad (11)$$

using the top-hat smoothing window function

$$W_{\text{top}}(x) = 2 \frac{J_1(x)}{x}, \quad (12)$$

where J_1 is the first Bessel function of the first kind.

We assume that the AP filtered kSZ temperature $\delta T_{\text{kSZ}}^{(\text{AP})}$ associated with galaxy i is not affected by the other galaxies but only by the galaxy itself. Then, using equations (9) and (10), we obtain

$$\delta T_{\text{kSZ}}^{(\text{AP})}(\hat{n}_i) \simeq - \frac{T_0 \tau_i}{c} \vec{v}_{e,i} \cdot \hat{n}_i, \quad (13)$$

where the optical depth τ_i estimated at galaxy i is given by

$$\tau_i = \frac{\sigma_{\text{T}} N_{e,i}}{D_{A,i}^2} \int \frac{d^2\ell}{(2\pi)^2} U(\ell\theta_c) B(\vec{\ell}). \quad (14)$$

We simply take the gas-traces-mass assumption and admit the universalities of the gas-mass fraction f_{gas} and the host halo mass M for galaxies, resulting in $N_e \sim f_{\text{gas}} M / (\mu_e m_p)$, where $\mu_e = 1.17$ is the mean particle weight per electron, and m_p is the proton mass. We estimate the angular diameter distance at effective redshift z_{eff} of a given galaxy sample. Then, the optical depth becomes the approximately-same at each galaxy: $\tau = \tau_i$, where τ is interpreted as an ‘‘average’’ optical depth that is a proportionality constant to fit the observed kSZ temperature to the prediction of the LOS peculiar velocity. This estimation corresponds to the assumption that there is no strong correlation between the optical depth and the peculiar velocity for a given galaxy (halo). In addition, we assume that the peculiar velocity of free electrons can be regarded as the velocity of dark matter: $\vec{v} = \vec{v}_e$. Under the above assumptions, the relation between the kSZ temperature and the LOS peculiar velocity simplifies to

$$\delta T_{\text{kSZ}}^{(\text{AP})}(\hat{n}_i) = - \frac{T_0 \tau}{c} \vec{v}_i \cdot \hat{n}_i, \quad (15)$$

where the average optical depth is given by

$$\tau = \frac{\sigma_{\text{T}} f_{\text{gas}} M}{\mu_e m_p D_A^2(z_{\text{eff}})} \int \frac{d^2\ell}{(2\pi)^2} U(\ell\theta_c) B(\vec{\ell}). \quad (16)$$

Most of the electrons in the halo are in ionized gas and are traced by the kSZ effect. We expect that only a small fraction of the mass is in neutral gas and stars (Fukugita & Peebles 2004). Therefore, we expect that the value of the gas fraction f_{gas} is similar to the universal baryon fraction $f_b = \Omega_b / \Omega_m = 0.155$, which is tightly constrained at high redshift by measurements of CMB (Hinshaw et al. 2013; Planck Collaboration et al. 2016c) and of the abundance of light elements formed through the process of Big Bang nucleosynthesis (BBN) (Steigman 2007).

3.1.2 Realistic Gas profiles

We now relax the point source assumption and allow the gas in galaxies to have an extended profile. However, for the LOWZ and CMASS halos the exact shape of the gas profile that induces the kSZ effect is currently very uncertain. In this work, we assume that on average the gas profile can be expressed as a projected gas profile $N(\vec{\theta})$, and that the kSZ temperature is expressed as the convolution of the point source kSZ temperature with an assumed gas profile function. Then, we finally derive the optical depth model assuming the gas-profile

$$\tau = \frac{\sigma_{\text{T}} f_{\text{gas}} M}{\mu_e m_p D_A^2(z_{\text{eff}})} \int \frac{d^2\ell}{(2\pi)^2} U(\ell\theta_c) N(\vec{\ell}) B(\vec{\ell}), \quad (17)$$

where $N(\vec{\ell})$ is the Fourier transform of an assumed projected gas profile. In the following analysis we consider two functional forms for the projected gas profiles, (1) a Gaussian profile with a characteristic radius, σ_R (Schaan et al. 2016) and (2) a β -profile with slope β and core radius θ_R (Cavaliere & Fusco-Femiano 1976), given by

$$N_G(\theta) = \frac{1}{2\pi\sigma_R^2} e^{-\theta^2/(2\sigma_R^2)}$$

$$N_\beta(\theta) = N_0 \left(1 + \frac{\theta^2}{\theta_R^2}\right)^{-\frac{3}{2}\beta + \frac{1}{2}}, \quad (18)$$

where N_0 is the normalization factor so that $\int d^2\theta N_\beta(\theta) = 1$. Furthermore, we use the Gaussian beam function, $B(\ell) = e^{-\sigma_B^2 \ell^2/2}$.

For the Gaussian gas profile, we can derive a simple analytic form of the optical depth as follows

$$\tau = \frac{\sigma_T f_{\text{gas}} M}{2\pi\mu_e m_p \Sigma^2 D_A^2(z_{\text{eff}})} \quad (19)$$

with

$$\Sigma^2 = \frac{(4\sigma_B^2 + 4\sigma_R^2 + \theta_c^2)(2\sigma_B^2 + 2\sigma_R^2 + \theta_c^2)}{4\theta_c^2}, \quad (20)$$

where we assumed that the top-hat smoothing window function $W_{\text{top}}(x)$ (equation 12) is a Gaussian function $W_{\text{top}}(x) \sim e^{-(x/2)^2/2}$. We note here that the optical depth has the maximum value at an aperture radius of

$$\theta_{\text{peak}} = 2^{3/4} \sqrt{\sigma_B^2 + \sigma_R^2}. \quad (21)$$

At the peak, we obtain

$$\Sigma^2 = 2.914 (\sigma_B^2 + \sigma_R^2), \quad (22)$$

and we find that the amplitude of the kSZ signal is reduced by a factor of 3 due to the AP filtering, because we obtain $\Sigma^2 = \sigma_B^2 + \sigma_R^2$ if we do not apply the filtering. For an optimal aperture radius computed by equation (21), we can estimate a typical value of the optical depth as follows

$$\tau = 5.37 \times 10^{-5} \left(\frac{f_{\text{gas}}}{0.155}\right) \left(\frac{M}{10^{14} h^{-1} M_\odot}\right) \times \left(\frac{h}{0.68}\right) \left(\frac{3'}{\sqrt{\sigma_B^2 + \sigma_R^2}}\right)^2 \left(\frac{10^3 h^{-1} \text{Mpc}}{D_A}\right)^2. \quad (23)$$

A typical value of the characteristic radius σ_R in the Gaussian gas profile can be estimated from the halo radius R divided by the angular diameter distance D_A : $\sigma_R = R/D_A$. A way of estimating the halo radius R through the halo mass M is

$$R_\Delta = \left(\frac{3}{4\pi} \frac{M}{\Delta \rho_{\text{crit}}(z)}\right)^{1/3}, \quad (24)$$

where R_Δ is the radius within which the average density of the halo is Δ times larger than the critical density $\rho_{\text{crit}}(z)$ at redshift z . When we choose $\Delta = 200$, we estimate the mean halo radii of $R_{200} = 0.54 h^{-1} \text{Mpc}$ for LOWZ and $R_{200} = 0.39 h^{-1} \text{Mpc}$ for CMASS, which respectively correspond to $\sigma_R = 2.7'$ and $1.4'$. Since the beam size for the WPR2 map is $\sigma_B = 2.1'$, the LOWZ halos can be resolved, while the CMASS halos cannot. The peak position of the AP filtered optical depth is estimated as $\theta_{\text{peak}} = 4.9'$ for LOWZ and $\theta_{\text{peak}} = 4.0'$ for CMASS. It is worth noting that

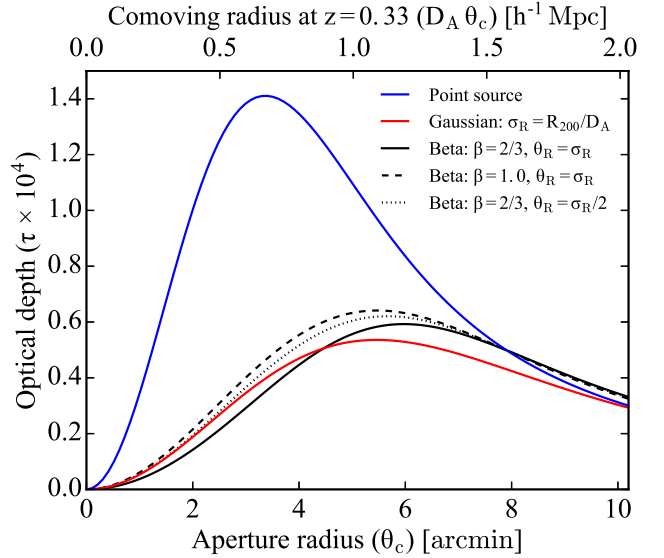


Figure 1. Optical depth as a function of the angular radius θ_c of the AP filter for various gas profiles (equation 17). We use the parameters that correspond to the LOWZ sample and the WPR2 map (Sec. 2): $M = 5.2 \times 10^{13} h^{-1} M_\odot$, $z = 0.33$, $\text{FWHM} = 5'$, $h = 0.68$, $\sigma_R = R_{200}/D_A$, and $f_{\text{gas}} = 0.155$. The optical depth amplitudes computed by both the Gaussian profile (red solid) and the β -profile with different three parameters (black solid, black dashed, black dotted) are smaller than that computed by the point source assumption, and the peak positions predicted by the gas profiles shift outward compared to the point source prediction.

the Gaussian profile includes the point source assumption in the limit of $\sigma_R \rightarrow 0$, leading to a peak position of $\theta_{\text{peak}} = 3.6'$ for both LOWZ and CMASS. From equations (23) and (24), we find that for $\sigma_B \gg \sigma_R$ the optical depth is proportional to the mean halo mass M divided by the square of the angular diameter distance $(D_A(z))^2$, while for $\sigma_B \ll \sigma_R$ the optical depth is proportional to $M^{1/3}$ multiplied by $(\rho_{\text{crit}}(z))^{2/3}$. In other words, the optical depth decreases with increasing redshift for the former case ($\sigma_B \gg \sigma_R$), while it increases for the latter case ($\sigma_B \ll \sigma_R$). Thus, we expect that future kSZ surveys with high-resolution CMB experiments that satisfy $\sigma_B \ll \sigma_R$ such as Advanced ACTPol (Calabrese et al. 2014; Henderson et al. 2016) and CMB-S4 (Abazajian et al. 2015) will allow us to detect high-redshift kSZ signals. (See Section 8 for details.)

For the β -profile, the integral in the normalization factor $1/N_0 = \int d^2\theta (1 + \theta^2/\theta_R^2)^{-\frac{3}{2}\beta + \frac{1}{2}}$ has a logarithmic divergence and needs to be truncated; therefore, the optical depth predicted from the β -profile significantly depends on the upper limit of the integral θ_{max} . For a fair comparison with the Gaussian profile, we choose $\theta_{\text{max}} = 2\sigma_R$, because 95 percent of the total number of electrons associated with a given halo is distributed within $2\sigma_R$ in the Gaussian profile.

Fig. 1 shows the optical depth as a function of aperture radius θ_c for various gas profile models (see also Schaan et al. 2016, Fig. 1). We use equation (17) with the following parameters that correspond to the LOWZ sample and the WPR2 map: $M = 5.2 \times 10^{13} h^{-1} M_\odot$, $z = 0.33$, $\text{FWHM} = 5'$, $h = 0.68$, $\sigma_R = R_{200}/D_A$, and $f_{\text{gas}} = 0.155$. For small θ_c , the kSZ signal contributes to the disk and the ring of the AP filter, which leads to a cancellation. For large θ_c , the kSZ

signal is entirely included in the disk of the AP filter, and the AP filtered optical depth has a peak, depending on the CMB resolution σ_B and the gas radius σ_R in equation (21). The amplitudes of the optical depth predicted from the Gaussian- and β -profiles (red and black lines) are smaller than that computed from the point source assumption (blue line), and the peak positions predicted by the gas profiles shift outward compared to the point source prediction.

3.2 Pairwise kSZ power spectra and correlation functions

In this work, we apply the kSZ power spectrum approach developed in (Sugiyama et al. 2016a). We compute the kSZ power spectrum on the aperture-averaged data,

$$P_{\text{kSZ}}(\vec{k}) = \left\langle -\frac{V}{N^2} \sum_{i,j} [\delta T_{\text{kSZ}}^{(\text{AP})}(\hat{n}_i) - \delta T_{\text{kSZ}}^{(\text{AP})}(\hat{n}_j)] e^{-i\vec{k}\cdot\vec{s}_{ij}} \right\rangle, \quad (25)$$

where \vec{s}_i denotes the position of galaxy i in the survey, $\vec{s}_{ij} = \vec{s}_i - \vec{s}_j$, N represents the total number of observed galaxies, and V is the survey volume. The redshift-space position, \vec{s}_i , is displaced from the real-space galaxy coordinate, x_i , by the velocity along the LOS:

$$\vec{s}_i = \vec{x}_i + \frac{\vec{v}_i \cdot \hat{n}_i}{aH} \hat{n}_i, \quad (26)$$

where \hat{n}_i is the LOS, and H is the Hubble parameter. The pairwise kSZ power spectrum is the Fourier transform of the pairwise kSZ correlation function:

$$\xi_{\text{kSZ}}(\vec{s}) = \left\langle -\frac{V}{N^2} \sum_{i,j} [\delta T_{\text{kSZ}}^{(\text{AP})}(\hat{n}_i) - \delta T_{\text{kSZ}}^{(\text{AP})}(\hat{n}_j)] \delta_{\text{D}}(\vec{s} - \vec{s}_{ij}) \right\rangle. \quad (27)$$

One can see from equation (15) that P_{kSZ} and ξ_{kSZ} are respectively proportional to the LOS pairwise velocity power spectrum, P_{pv} , and correlation function, ξ_{pv} ,

$$\begin{aligned} P_{\text{kSZ}}(\vec{k}) &\simeq \left(\frac{T_0 \tau}{c} \right) P_{\text{pv}}(\vec{k}), \\ \xi_{\text{kSZ}}(\vec{s}) &\simeq \left(\frac{T_0 \tau}{c} \right) \xi_{\text{pv}}(\vec{s}), \end{aligned} \quad (28)$$

where

$$\begin{aligned} P_{\text{pv}}(\vec{k}) &= \left\langle \frac{V}{N^2} \sum_{i,j} [\vec{v}_i \cdot \hat{n}_i - \vec{v}_j \cdot \hat{n}_j] e^{-i\vec{k}\cdot\vec{s}_{ij}} \right\rangle, \\ \xi_{\text{pv}}(\vec{s}) &= \left\langle \frac{V}{N^2} \sum_{i,j} [\vec{v}_i \cdot \hat{n}_i - \vec{v}_j \cdot \hat{n}_j] \delta_{\text{D}}(\vec{s} - \vec{s}_{ij}) \right\rangle. \end{aligned} \quad (29)$$

The LOS pairwise velocity power spectrum and correlation function can be also defined using the density-weighted velocity field of galaxies, which is often referred to as the ‘‘momentum field’’ (e.g., Park (2000)). The LOS momentum field is defined as $p(\vec{x}) = [\vec{v}(\vec{x}) \cdot \hat{n}](1 + \delta(\vec{x}))$ in real space, where δ is the density contrast, and the translation of $p(\vec{x})$ from real space to redshift space is given by (Okumura et al. 2014; Sugiyama et al. 2016b)

$$p_s(\vec{s}) = \int d^3x [\vec{v}(\vec{x}) \cdot \hat{n}](1 + \delta(\vec{x})) \delta_{\text{D}}\left(\vec{s} - \vec{x} - \frac{\vec{v}(\vec{x}) \cdot \hat{n}}{aH} \hat{n}\right), \quad (30)$$

where the subscript ‘‘s’’ denotes a quantity defined in redshift space. Then, P_{pv} and ξ_{pv} are represented as

$$\begin{aligned} (2\pi)^3 \delta_{\text{D}}(\vec{k} + \vec{k}') P_{\text{pv}}(\vec{k}) &= \langle p_s(\vec{k}) \delta_s(\vec{k}') - \delta_s(\vec{k}) p_s(\vec{k}') \rangle \\ \xi_{\text{pv}}(\vec{s}_1 - \vec{s}_2) &= \langle p_s(\vec{s}_1) \delta_s(\vec{s}_2) - \delta_s(\vec{s}_1) p_s(\vec{s}_2) \rangle, \end{aligned} \quad (31)$$

where δ_s is the redshift-space density contrast.

In our recent studies (Sugiyama et al. 2016b; Sugiyama et al. 2016a), we have shown that the LOS pairwise velocity power spectrum including the RSD effect is related to the galaxy power spectrum in redshift space $P_s(\vec{k})$ under the global plane parallel approximation $\hat{n}_i \sim \hat{n}_j \sim \hat{n}$,¹

$$P_{\text{pv}}(\vec{k}) = \left(i \frac{aH}{\vec{k} \cdot \hat{n}} \right) \frac{\partial}{\partial \gamma} P_s(\vec{k}; \gamma \vec{v}) \Big|_{\gamma=1}, \quad (32)$$

where the dependence of $P_s(\vec{k})$ on peculiar velocity that causes RSDs is schematically represented as $P_s(\vec{k}; \vec{v})$. This relation can be easily shown by substituting the particle description of the galaxy power spectrum

$$P_s(\vec{k}) = \left\langle \frac{V}{N^2} \sum_{i,j} e^{-i\vec{k}\cdot\vec{s}_{ij}} \right\rangle \quad (33)$$

into equation (32), where \vec{s}_i is the redshift-space coordinates (equation 26).

It is worth noting that the relation in equation (32) is quite general and holds without any assumption except for the global plane parallel approximation. If dark matter obeys the system of equations for a pressure-less perfect fluid without vorticity, and if $f = \Omega_m^{1/2}$, where f denotes the linear growth rate, we can solve the equations using cosmological perturbation theory. These assumptions lead to separable solutions of redshift z (or the linear growth function $D(z)$) and wavevector \vec{k} to arbitrary order in perturbation theory, resulting in that the perturbation theory solution of the velocity field is proportional to the linear growth rate to any order: $\vec{v} \propto f$ (or $f\sigma_8$) (Bernardeau et al. 2002). Since the approximation that $f \approx \Omega_m^{0.557-0.02z}$ is accurate to 0.3% (Polarski & Gannouji 2008), the separable solutions in non-linear perturbation theories have been widely used. Then, equation (32) is simplified to

$$P_{\text{pv}}(\vec{k}) = \left(i \frac{aHf}{\vec{k} \cdot \hat{n}} \right) \frac{\partial}{\partial f} P_s(\vec{k}; \vec{v}). \quad (34)$$

The above relation holds even if the linear growth rate f is replaced by $f\sigma_8$. These relations in equations (32) and (34) can be applied to any object such as dark matter particles, halos, galaxies, and galaxy clusters; furthermore, they could be used to compute the LOS pairwise velocity power spectrum when we use any cosmological perturbation theory: e.g., the standard perturbation theory (Bernardeau et al. 2002), the Lagrangian perturbation theory (Matsubara 2008; Carlson et al. 2013; Sugiyama 2014), the effective field theory approach (Baumann et al. 2012; Carrasco et al. 2012), the distribution function approach (Seljak & McDonald 2011), and the TNS model (Taruya et al. 2010).

We compute the LOS pairwise velocity power spectrum in linear perturbation theory (Okumura et al. 2014;

¹ While equation (32) represents the redshift-space P_{pv} , the real-space one without including the RSD effect can be given by taking $\gamma = 0$ in equation (32) (see also Scoccimarro (2004)):

$$P_{\text{pv}}(\vec{k}) = \left(i \frac{aH}{\vec{k} \cdot \hat{n}} \right) \frac{\partial}{\partial \gamma} P_s(\vec{k}; \gamma \vec{v}) \Big|_{\gamma=0}.$$

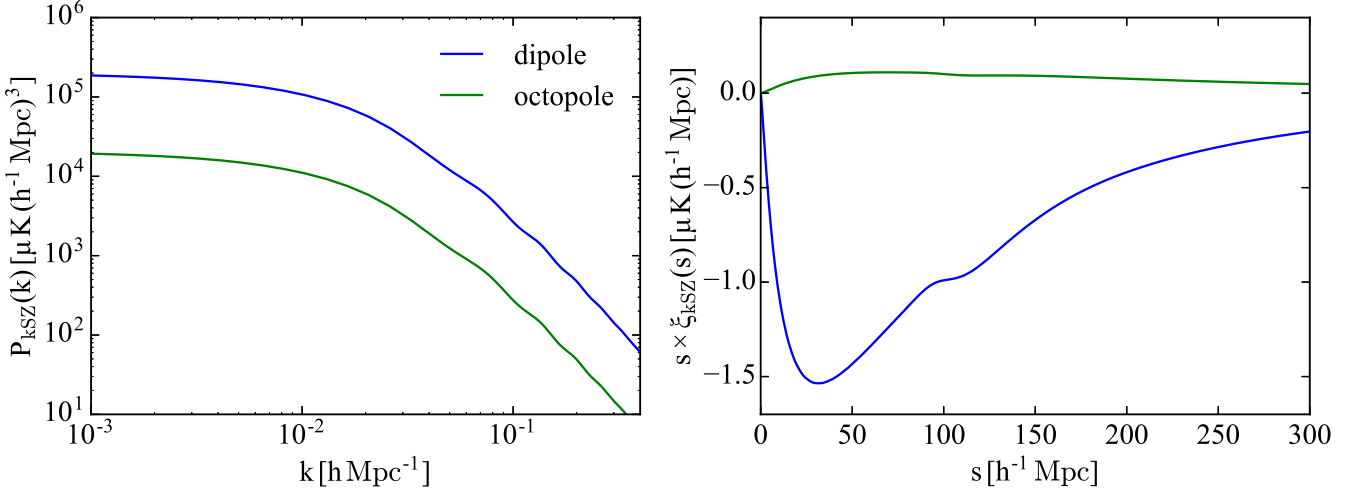


Figure 2. Dipoles ($\ell = 1$) and octopoles ($\ell = 3$) of both the pairwise kSZ power spectrum (left panel) and correlation function (right panel) for the LOWZ sample. We adopt the fiducial values of $f\sigma_8 = 0.392$ and $b\sigma_8 = 1.283$ and the best-fitting value of the optical depth obtained from our kSZ analysis (Sec. 7.2), $\tau E = 3.95 \times 10^{-5}$. The dipole is about 10 times larger than the octopole.

Sugiyama et al. 2016b). Using equation (34), we derive

$$\begin{aligned} P_{\text{pv}}(\vec{k}) &= \left(i \frac{aHf}{\vec{k} \cdot \hat{n}} \right) \frac{\partial}{\partial f} (b + f\mu^2)^2 D^2 P_{\text{lin}}(k) \\ &= 2iaHf\mu (b + f\mu^2) D^2 \frac{P_{\text{lin}}(k)}{k}, \end{aligned} \quad (35)$$

where $(b + f\mu^2)$ is the linear Kaiser factor (Kaiser 1987), $\mu = \hat{k} \cdot \hat{n}$, b is the linear bias, and P_{lin} is the linear matter power spectrum at the present time. Similarly to the RSD analysis of the galaxy power spectrum (as the latest result, see Alam et al. (2016) and references therein), we expand P_{pv} in Legendre polynomials \mathcal{L}_ℓ ,

$$P_{\text{pv}, \ell}(k) = (2\ell + 1) \int \frac{d\Omega_k}{4\pi} \mathcal{L}_\ell(\mu) P_{\text{pv}}(\vec{k}), \quad (36)$$

where $d\Omega_k$ is the solid angle element in k -space. In the linear theory limit, the pairwise kSZ power multipoles become zero except for $\ell = 1$ and 3, and using equations (28), (35), and (36), we finally have,

$$\begin{aligned} P_{\text{kSZ}, \ell=1}(k) &= 2i \frac{T_0 H_0}{c} (a\tau E) \left[(f\sigma_8)(b\sigma_8) + \frac{3}{5} (f\sigma_8)^2 \right] \frac{P_{\text{lin}}(k)}{k} \\ P_{\text{kSZ}, \ell=3}(k) &= 2i \frac{T_0 H_0}{c} (a\tau E) \left[\frac{2}{5} (f\sigma_8)^2 \right] \frac{P_{\text{lin}}(k)}{k}, \end{aligned} \quad (37)$$

where $E(z) = H(z)/H_0$, which is given by $E(z) = \sqrt{(1+z)^3 \Omega_m + \Omega_\Lambda}$ in a flat Λ CDM model, and we normalize the linear power spectrum using σ_8 at the present time: $P_{\text{lin}}(k) \rightarrow P_{\text{lin}}(k)/\sigma_8^2(z=0)$. It is worth noting that the pairwise kSZ power constrains τE , not τ , where the growth rate $f\sigma_8$ and the linear bias $b\sigma_8$ are well constrained from the RSD analysis of galaxy clustering: $f\sigma_8 = 0.392$ (0.445) and $b\sigma_8 = 1.283$ (1.218) for the LOWZ (CMASS) sample (Gil-Marín et al. 2016). In contrast to the galaxy power spectrum that is real and contains only even multipoles, the pairwise kSZ power spectrum is imaginary and contains only odd multipoles.

The inverse Fourier transform of the pairwise kSZ power multipoles leads to the analytic form of the pairwise kSZ

correlation function

$$\xi_{\text{kSZ}, \ell}(s) = i^\ell \int \frac{dk k^2}{2\pi^2} j_\ell(k s) P_{\text{kSZ}, \ell}(k), \quad (38)$$

where $j_\ell(k s)$ is the spherical Bessel function of order ℓ . In linear theory, we obtain from equation (37)

$$\begin{aligned} \xi_{\text{kSZ}, \ell=1}(s) &= -2 \frac{T_0 H_0}{c} (a\tau E) \left[(f\sigma_8)(b\sigma_8) + \frac{3}{5} (f\sigma_8)^2 \right] \xi'_{\ell=1}(s) \\ \xi_{\text{kSZ}, \ell=3}(s) &= 2 \frac{T_0 H_0}{c} (a\tau E) \left[\frac{2}{5} (f\sigma_8)^2 \right] \xi'_{\ell=3}(s), \end{aligned} \quad (39)$$

where

$$\xi'_\ell(s) = \int \frac{dk k^2}{2\pi^2} j_\ell(k s) \frac{P_{\text{lin}}(k)}{k}. \quad (40)$$

We find that the pairwise kSZ dipole, $\xi_{\text{kSZ}, \ell=1}$, is negative in linear theory. This means that gravitational attraction predicts a slight tendency of any pair of galaxies to be moving toward rather than away from each other at large scales, where we follow the convention that if two galaxies are moving toward each other, their contribution to the pairwise velocity is negative. The linear Kaiser effect from RSDs increases the amplitude of the pairwise kSZ dipole by $\sim 20\%$ for both LOWZ and CMASS at linear regimes. On the other hand, at non-linear small scales RSDs displace galaxies away from each other, and thus, in redshift space the sign of $\xi_{\text{kSZ}, \ell=1}$ changes around $10 h^{-1} \text{ Mpc}$ ($k \simeq 0.2 h \text{ Mpc}^{-1}$) from negative to positive (Okumura et al. 2014; Sugiyama et al. 2016b; Sugiyama et al. 2016a). This small-scale effect of RSDs is analogous to the Finger-of-God (FoG) effect but is not the same, because we have shown that this change in sign of $\xi_{\text{kSZ}, \ell=1}$ appears even in the Zel'dovich approximation that does not form halos (Sugiyama et al. 2016b). Therefore, it could be considered that the change in sign of $\xi_{\text{kSZ}, \ell=1}$ is caused by non-linear velocity dispersion effects, part of which is the FoG effect. The latest kSZ measurement using the high resolution ACT data (De Bernardis et al. 2016) clearly shows the expected change in sign of the pairwise velocity at $\sim 10 h^{-1} \text{ Mpc}$.

Fig. 2 shows the theoretical predictions of the pairwise kSZ dipole and octopole in linear theory (equations 37 and 39) for the LOWZ sample ($f\sigma_8 = 0.392$ and $b\sigma_8 = 1.283$), where we use the best fit value of the optical depth, $\tau E = 3.95 \times 10^{-5}$, estimated from our kSZ measurement (Sec. 7.2). Since this figure shows the linear theory results that we use in our analysis, the change in sign of $\xi_{\text{kSZ}, \ell=1}$ around $\sim 10 h^{-1}$ Mpc does not occur unlike non-linear theories (Okumura et al. 2014; Sugiyama et al. 2016b). As the shape of the pairwise kSZ power spectrum is proportional to $P_{\text{lin}}(k)/k$, the amplitude increases at large scales. As the data improves, we will be able to investigate the pairwise kSZ signal at larger scales than $\sim 200 h^{-1}$ Mpc (e.g. De Bernardis et al. 2016, Fig. 3). While the data should show a baryon acoustic peak around $\sim 100 h^{-1}$ Mpc in the linear theory prediction of $\xi_{\text{kSZ}, \ell=1}$ (see blue line in the right panel of Fig. 2), the peak is significantly broadened by non-linear effects (Sugiyama et al. 2016b). The octopole, which is generated from the RSD effect and is free of the linear bias, is about 10 times smaller than the dipole. In future kSZ measurements such as Advanced ACTPol and CMB-S4, we will want to measure all of the multipoles up to the octopole. This full measurement will constrain cosmological parameters, especially for the linear growth rate $f\sigma_8$ and the Hubble expansion parameter H (Sugiyama et al. 2016a). However, the data used in this work is too noisy to detect the octopole; therefore, we do not analyze it in what follows. In this paper, we measure the pairwise kSZ power dipole $P_{\text{kSZ}, \ell=1}$ and constrain the optical depth value τE after fixing all the other parameters.

3.3 Comparison with previous works

It is well known that the commonly used pairwise velocity $v_{\text{pair}}(r)$ is related to the time derivative of the galaxy two-point correlation function $\xi_{\text{g}}(r)$ under the following three assumptions: pair conservation of galaxies, isotropic peculiar velocities, and isotropic clustering of galaxies (Peebles 1976; Davis & Peebles 1977; Peebles 1980),

$$v_{\text{pair}}(r) = -\frac{\int_0^r dr' r'^2 \frac{\partial}{\partial t} \xi_{\text{g}}(r')}{r^2 (1 + \xi_{\text{g}}(r))}. \quad (41)$$

Since the total number of galaxies is not conserved, and since we measure the LOS velocity via the kSZ effect in anisotropic galaxy clustering by RSDs, it will not be possible to apply the above expression to the kSZ analysis directly. We stress here that the relations presented in equations (32) and (34) hold without any of these three assumptions.

The dipole of the pairwise kSZ correlation function $\xi_{\text{kSZ}, \ell=1}$ is closely related to the mean pairwise velocity v_{pair} (equation 41) estimated from the previous kSZ measurements (Hand et al. 2012; Planck Collaboration et al. 2016a; Soergel et al. 2016; De Bernardis et al. 2016). The pairwise velocity v_{pair} is computed by the pair-weighted average with the weight factor $n_1 n_2 / \langle n_1 n_2 \rangle$, where n_1 and n_2 are the number density fields at points \vec{x}_1 and \vec{x}_2 , and $\langle n_1 n_2 \rangle$ yields the galaxy two-point correlation function ξ_{g} . On the other hand, we replace the denominator of the pair-weighted average $\langle n_1 n_2 \rangle$ by the square of the mean number density \bar{n}^2 . Thus, our approach does not need an additional calculation of ξ_{g} in modeling $\xi_{\text{kSZ}, \ell}$ (see Okumura et al. (2014) for the

detailed discussion of the difference between pair-weighted and density-weighted velocities).

Keisler & Schmidt (2013) noted that the kSZ signal is proportional to $\tau b f \sigma_8^2$ and can be used to break the degeneracy between f and σ_8 that appears in the RSD analysis of galaxy clustering. On the other hand, in our analysis the pairwise kSZ dipole is proportional to $\tau [(b\sigma_8)(f\sigma_8) + \frac{3}{5}(f\sigma_8)^2]$ due to the RSD effect, and we fix $f\sigma_8$ and $b\sigma_8$ from the RSD analysis; therefore, the degeneracy between f and σ_8 cannot be broken.

4 METHODOLOGY

4.1 Galaxy and kSZ density fluctuations

We estimate the filtered CMB temperature $T_{\text{AP}}(\hat{n}_i)$ associated with galaxy i by applying the AP filter (Sec. 3.1). Using HEALPIX, we firstly find pixels that lie within a disk of radius, θ_c , around each galaxy and average the temperature within the disk. Next, we compute the mean temperature in a surrounding ring of inner and outer radii and subtract it from the mean temperature within the disk, where the outer radius is chosen to be $\sqrt{2}\theta_c$. Finally, we define the filtered CMB temperature fluctuation $\delta T_{\text{AP}}(\hat{n}_i)$ by subtracting the average of $T_{\text{AP}}(\hat{n}_i)$ obtained from all galaxies after weighting by w_c from $T_{\text{AP}}(\hat{n}_i)$:

$$\delta T_{\text{AP}}(\hat{n}_i) = T_{\text{AP}}(\hat{n}_i) - \frac{\sum_i^{N_{\text{gal}}} T_{\text{AP}}(\hat{n}_i) w_c(\vec{s}_i)}{\sum_i^{N_{\text{gal}}} w_c(\vec{s}_i)}. \quad (42)$$

where w_c is the completeness weight defined in equation (1).

The fluctuations of three-dimensional galaxy and kSZ density fields are then given by

$$\begin{aligned} \delta n(\vec{s}) &= \sum_i^{N_{\text{gal}}} w_c(\vec{s}_i) \delta_{\text{D}}(\vec{s} - \vec{s}_i) - \alpha \sum_i^{N_{\text{ran}}} \delta_{\text{D}}(\vec{s} - \vec{s}_i), \\ \delta T(\vec{s}) &= \sum_i^{N_{\text{gal}}} \delta T_{\text{AP}}(\hat{n}_i) w_c(\vec{s}_i) \delta_{\text{D}}(\vec{s} - \vec{s}_i), \end{aligned} \quad (43)$$

where N_{gal} and N_{ran} represent the numbers of galaxies in the real and synthetic catalogues, and the factor α is the ratio between the weighted numbers of galaxies in the galaxy and random catalogues, $\alpha = \sum_i^{N_{\text{gal}}} w_c(\vec{s}_i) / N_{\text{ran}} \sim 0.01$. Here we construct the fluctuations δn and δT so that their volume-averages become zero: $\int d^3s \delta T(\vec{s}) = \int d^3s \delta n(\vec{s}) = 0$.

Any evolution of contaminations of the kSZ signal, e.g. the tSZ effect and cosmic infrared background (CIB) emission, with redshift would result in a bias effect. Therefore, almost all the previous works compute the mean measured temperature weighing by a Gaussian kernel as a function of redshift, $G(z_i, z_j, \sigma_z) = \exp[-(z_i - z_j)^2 / (2\sigma_z^2)]$, and subtract it from the AP filtered temperature T_{AP} (Hand et al. 2012; Planck Collaboration et al. 2016a; Soergel et al. 2016; De Bernardis et al. 2016) to obtain an unbiased estimate of the kSZ signal. However, since there is minimal CIB contamination in the WPR2 maps (Bobin et al. 2016), we do not adopt this prescription. To validate our analysis, we compute the pairwise kSZ power spectrum using this prescription with $\sigma_z = 0.02$ and compare it to that without using the prescription. We have then checked that any residual CIB contamination is subdominant in our analysis and produces a small change in the pairwise kSZ power spectrum

estimates: the relative difference is $\leq 5\%$ at the scales of interest ($k < 0.15 h \text{ Mpc}^{-1}$).

4.2 Estimator of the Pairwise kSZ power multipoles

In analogy to the estimator of the galaxy power multipoles (Feldman et al. 1994; Yamamoto et al. 2006), we present an estimator of the pairwise kSZ power multipoles as,

$$\begin{aligned} \hat{P}_{\text{kSZ},\ell}(\vec{k}) &= -\frac{(2\ell+1)}{A} \int d^3 s_1 \int d^3 s_2 e^{-i\vec{k}\cdot\vec{s}_{12}} \mathcal{L}_\ell(\hat{k}\cdot\hat{n}_{12}) \\ &\times \left[\delta T(\vec{s}_1) \delta n(\vec{s}_2) - \delta n(\vec{s}_1) \delta T(\vec{s}_2) \right], \end{aligned} \quad (44)$$

where $\vec{s}_{12} = \vec{s}_1 - \vec{s}_2$ is the relative coordinates between two different points \vec{s}_1 and \vec{s}_2 , and the unit vector \hat{n}_{12} of $\vec{n}_{12} = (\vec{s}_1 + \vec{s}_2)/2$ is used as the LOS direction to the pair of points \vec{s}_1 and \vec{s}_2 . The normalization A is given by

$$A = \int d^3 s \bar{n}^2(\vec{s}), \quad (45)$$

where \bar{n} is the number density measured from the random catalogue, multiplied by α ,

$$\bar{n}(\vec{s}) = \alpha \sum_i^{N_{\text{ran}}} \delta_{\text{D}}(\vec{s} - \vec{s}_i). \quad (46)$$

The utility of the *pairwise estimator* is apparent in Fourier space, as the difference in the square bracket of equation (44), $\delta T(\vec{s}_1) \delta n(\vec{s}_2) - \delta n(\vec{s}_1) \delta T(\vec{s}_2)$, can be used to extract the imaginary elements of the pairwise kSZ power multipoles. We note here that the shot noise term does not appear in the pairwise estimator, as it is canceled out by the difference.

There are two main sources of noise in the pairwise kSZ signal, detector noise and primary CMB anisotropies. Integrating over \vec{s}_1 and \vec{s}_2 after weighting by odd-pole Legendre polynomials in the pairwise estimator (equation 44), these noise components will average to zero, because the parity of them is even, while the kSZ signal is odd parity. In other words, the noise contribution will not bias the imaginary part of the pairwise kSZ power multipoles, because they are scalar quantities, not a LOS component of the peculiar velocity vector such as the kSZ signal. While the noise does not contribute to the expectation value for the signal, it does contribute to its variance as we discuss in Appendix A.

In this paper, we apply the local plane parallel approximation:

$$\mathcal{L}_\ell(\hat{k}\cdot\hat{n}_{12}) \approx \mathcal{L}_\ell(\hat{k}\cdot\hat{s}_1) \approx \mathcal{L}_\ell(\hat{k}\cdot\hat{s}_2). \quad (47)$$

Then, this approximation allows the integrals in equation (44) to decouple into a product of Fourier transforms (Yamamoto et al. 2006; Blake et al. 2011; Beutler et al. 2014; Samushia et al. 2015):

$$\hat{P}_{\text{kSZ},\ell}(\mathbf{k}) = -\frac{(2\ell+1)}{A} [\delta T_\ell(\mathbf{k}) \delta n^*(\mathbf{k}) - \text{c.c.}], \quad (48)$$

where

$$\begin{aligned} \delta n(\mathbf{k}) &= \int d^3 s e^{-i\mathbf{k}\cdot\mathbf{s}} \delta n(\mathbf{s}) \\ \delta T_\ell(\mathbf{k}) &= \int d^3 s e^{-i\mathbf{k}\cdot\mathbf{s}} \mathcal{L}_\ell(\hat{k}\cdot\hat{s}) \delta T(\mathbf{s}). \end{aligned} \quad (49)$$

We note here that $\delta n(\mathbf{k})$ and $\delta T_\ell(\mathbf{k})$ can be built to be computable using any fast Fourier transform (FFT) algorithm (Bianchi et al. 2015; Scoccimarro 2015): therefore, the computation of the estimator will be $\mathcal{O}(N_k \log N_k)$, where N_k is the numbers of k -modes (for details, see Appendix B1).

Finally, we average the amplitude of the pairwise kSZ power multipoles measured from equation (48) in spherical shell of \vec{k} to produce our estimate of $\hat{P}_{\text{kSZ},\ell}(k)$ at each bin $k = |\vec{k}|$:

$$\begin{aligned} \hat{P}_{\text{kSZ},\ell}(k) &= \int \frac{d\Omega_k}{4\pi} \hat{P}_{\text{kSZ},\ell}(\vec{k}) \\ &= \frac{1}{N_{\text{mode}}} \sum_{k-\frac{\Delta k}{2} < k < k+\frac{\Delta k}{2}} \hat{P}_{\text{kSZ},\ell}(\vec{k}), \end{aligned} \quad (50)$$

where N_{mode} is the number of independent Fourier modes in a k -bin.

4.3 Prescription of Measurements

Gil-Marín et al. (2016) computed the galaxy power spectra at the NGC and SGC and combined them by weighting by their effective area. Since we use the values of $f\sigma_8$ and $b\sigma_8$ measured from the RSD analysis of galaxy clustering in Gil-Marín et al. (2016), for consistency we compute the combined pairwise kSZ power multipoles

$$P_{\text{kSZ},\ell}(k) = \left(A_{\text{NGC}} P_{\text{kSZ},\ell}^{\text{(NGC)}} + A_{\text{SGC}} P_{\text{kSZ},\ell}^{\text{(SGC)}} \right) / (A_{\text{SGC}} + A_{\text{NGC}}), \quad (51)$$

where A_{NGC} and A_{SGC} are the effective areas of the NGC and SGC, respectively, whose values are $A_{\text{NGC}}^{\text{LOWZ}} = 5836 \text{ deg}^2$, $A_{\text{SGC}}^{\text{LOWZ}} = 2501 \text{ deg}^2$, $A_{\text{NGC}}^{\text{CMASS}} = 6851 \text{ deg}^2$, and $A_{\text{SGC}}^{\text{CMASS}} = 2525 \text{ deg}^2$. In the following analysis we perform the parameter fitting process to the combined NGC+SGC power spectrum.

We define the Cartesian coordinates $\vec{s} = (x, y, z)$ with z being the axis toward the north pole. We place the LOWZ and CMASS samples in a cuboid of dimensions (L_x, L_y, L_z) , where $(L_x, L_y, L_z) [h^{-1} \text{ Mpc}] = (2400, 4200, 2400)$ for CMASS-NGC, $(2600, 3400, 2000)$ for CMASS-SGC, $(2300, 4000, 2300)$ for LOWZ-NGC, and $(2400, 3200, 1700)$ for LOWZ-SGC. The CMASS and LOWZ galaxies are distributed on the FFT grid using the triangular-shaped cloud (TSC) assignment function. We use the Fast Fourier Transform in the West (FFTW)² with a 512 grid on each axis. This corresponds to a grid-cell resolution of $\sim 5 h^{-1} \text{ Mpc}$ for both CMASS and LOWZ. We have checked that for the scales of interest ($k < 0.15 h \text{ Mpc}^{-1}$), doubling the number of grid-cells per side, from 512 to 1024, produces a small change in the pairwise kSZ power spectrum estimated by equation (48), within 0.3%.

The FFT algorithm requires the interpolation of functions on a regular grid in position space. This interpolation results in the so-called aliasing effect (e.g. Jing (2005)). To reduce the aliasing effect, we adopt a simple technique proposed by (Hockney R. W. 1981; Sefusatti et al. 2016) that is based on the interlacing of two grids (for details, see Appendix B2).

In our analysis, we do not take account of the binning

² <http://fftw.org>

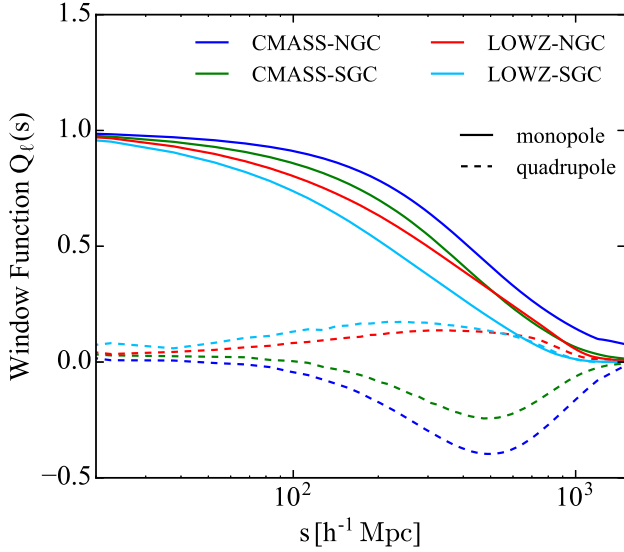


Figure 3. Multipoles of survey window function for BOSS DR12 as given in equation (C7), which are used to compute the masked pairwise kSZ power dipole in equation (54). The coloured lines display the window functions for CMASS-NGC (blue), CMASS-SGC (green), LOWZ-NGC (red), and LOWZ-SGC (cyan). The solid and dashed lines denote the monopole and quadrupole, respectively. The monopole effect decreases with increasing survey volumes, so that the monopole Q_0 becomes close to unity. The quadrupole Q_2 represents survey geometry anisotropies along radial directions, and its shape depends on a given survey: e.g. the quadrupole is positive for LOWZ and is negative for CMASS.

discreteness. It is evident at low k and may introduce systematic biases into the kSZ power estimate at a few percent level. We defer a more detailed analysis investigating this effect for future kSZ measurements.

5 SURVEY WINDOW FUNCTIONS

The imprint of survey geometry yields systematic differences between the observed pairwise kSZ power spectrum and their theoretical predictions presented in Sec. 3.2. We follow the treatment of survey window functions suggested by Wilson et al. (2015) (see also Beutler et al. (2016)) and apply it to our kSZ analysis. While the survey window effect in the pairwise kSZ power spectrum is represented by a convolution integral in Fourier space, from the convolution theorem, the pairwise kSZ correlation function and the window function multiply to give the masked correlation function in configuration space. Therefore, we compute the masked pairwise kSZ power spectrum through a Hankel transform of the masked pairwise kSZ correlation function. In this section, we present the main equations, leaving their full derivations in Appendix C.

To characterize the distortion of the survey geometry, we define the survey window function multipoles in configuration space:

$$Q_\ell(s) = \frac{(2\ell+1)}{A} \int \frac{d\Omega_s}{4\pi} \int d^3 s_1 \int d^3 s_2 \delta_D(\vec{s} - \vec{s}_{12}) \times \mathcal{L}_\ell(\hat{s}_{12} \cdot \hat{s}_1) \bar{n}(\vec{s}_1) \bar{n}(\vec{s}_2), \quad (52)$$

where we used the local plane parallel approximation, $\hat{s}_1 \approx$

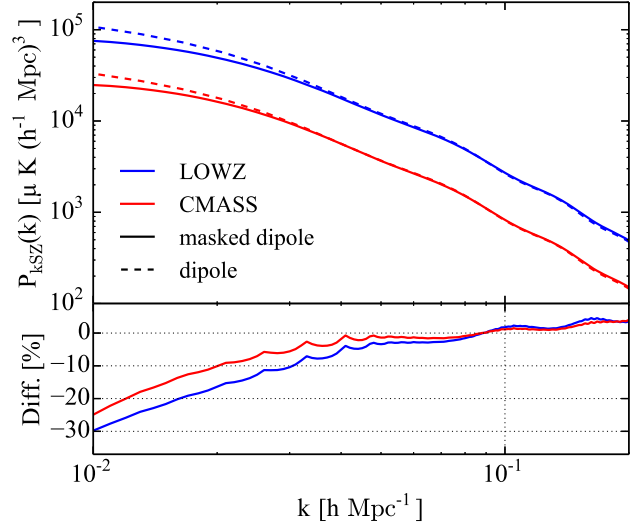


Figure 4. Theoretical predictions of the pairwise kSZ power dipole. The blue and red lines represent the results of LOWZ and CMASS, respectively. While the dashed lines show the true pairwise kSZ power dipole, the solid lines denote the masked results. Bottom panels show the relative differences: $P_{\text{masked}}/P_{\text{true}} - 1$. The window function effects are of order of 20-30% around $k = 0.01 h \text{ Mpc}^{-1}$.

\hat{s}_2 , and $\bar{n}(\vec{s})$ is the mean number density measured from the random catalogue (equation 46).

The masked (observed) pairwise kSZ power spectrum is expressed by the ensemble average of its estimator (equation 48), namely $\langle \hat{P}_{\text{kSZ}, \ell}(k) \rangle$. Using the window function multipoles, the masked pairwise kSZ power spectrum is given by (for derivation, see Appendix C)

$$\langle \hat{P}_{\text{kSZ}, \ell}(k) \rangle = 4\pi(-i)^\ell (2\ell+1) \int ds s^2 j_\ell(ks) \times \sum_{\ell_1 \ell_2} \begin{pmatrix} \ell & \ell_1 & \ell_2 \\ 0 & 0 & 0 \end{pmatrix}^2 \xi_{\text{kSZ}, \ell_1}(s) Q_{\ell_2}(s), \quad (53)$$

where the theoretical prediction of $\xi_{\text{kSZ}, \ell}$ is given by equation (39).³ For the pairwise kSZ power dipole, the necessary linear combination is obtained as

$$\langle \hat{P}_{\text{kSZ}, \ell=1}(k) \rangle = 4\pi(-i)^\ell \int ds s^2 j_{\ell=1}(ks) \times \xi_{\text{kSZ}, \ell=1}(s) \left(Q_0(s) + \frac{2}{5} Q_2(s) \right), \quad (54)$$

where in the right-hand-side the multipole expansion of the pairwise kSZ correlation function is truncated at the dipole, because higher multipoles (e.g. the octopole $\xi_{\text{kSZ}, \ell=3}$) are so small as to be ignored. This equation is the final expression of our template model to fit to the measurement of the pairwise kSZ power dipole.

The multipole components of the survey window function used in our analysis are shown in Fig. 3. The monopole Q_0 should become zero at the scales larger than the survey volume ($\sim 1 h^{-1} \text{ Gpc}$ for both CMASS and LOWZ),

³ It is worth noting that equation (53) reproduces equations (19) and (20) in Wilson et al. (2015) by replacing ξ_{kSZ} by the galaxy two-point correlation function ξ_g .

while on small scales where the survey edge effects no longer matter, it will be constant and will be equal to unity for an appropriate normalization A . Among the 4 regions of the BOSS, the correction derived from the monopole for CMASS-NGC is smallest while that for LOWZ-SGC largest. The quadrupole Q_2 , which represents survey geometry anisotropies along radial directions, will average to zero on both large and small scales. Its shape significantly depends on a given survey geometry: the quadrupole becomes positive and negative for LOWZ and CMASS, respectively.

Fig. 4 shows the theoretical predictions of the pairwise kSZ dipoles with the survey window corrections for both LOWZ and CMASS. The amplitude of the masked $P_{\text{kSZ}, \ell=1}$ becomes smaller than the true one at large scales, because we cannot find pairs of galaxies at scales larger than the survey volume. The window function effect is of order of 20-30% around $k \sim 0.01 h \text{ Mpc}^{-1}$ and significantly increases for $k < 0.01 h \text{ Mpc}^{-1}$.

6 COVARIANCE ESTIMATES

We estimate the data covariance matrix through resampling of data itself, using the delete one jackknife method (Quenouille 1956; Tukey 1958). After dividing the observed galaxy clustering data into N_{JK} spatial sub-regions on the sky, we define the resampling of the data by systematically omitting, in turn, each of N_{JK} sub-regions. To ensure that these regions cover approximately equal area, we employ the k -means algorithm⁴. To avoid underestimating clustering uncertainties, the resampling of the data should be applied on N_{JK} sub-regions into which the dataset has been split instead of on individual galaxies (Norberg et al. 2009). Unless otherwise specified, we employ $N_{\text{JK}} = 200$.

In the jackknife scheme, the covariance matrix is estimated by

$$C_{\text{JK}, ij} = \frac{N_{\text{JK}} - 1}{N_{\text{JK}}} \sum_k \left(y_i^k - \bar{y}_i \right) \left(y_j^k - \bar{y}_j \right), \quad (55)$$

where y_i^k is the i th measure of the statistic of interest for the k th configuration: in our analysis, $y_i = \hat{P}_{\text{kSZ}, \ell=1}(k_i)$. It is assumed that the mean expectation value \bar{y}_i is given by

$$\bar{y}_i = \frac{1}{N_{\text{JK}}} \sum_k y_i^k. \quad (56)$$

The inverse of the covariance matrix C_{JK}^{-1} estimated from data itself using the jackknife method is a biased estimator. To correct for this bias, we rescale the inverse covariance matrix as (Hartlap et al. 2007)

$$C^{-1} = \frac{N_{\text{JK}} - N_{\text{bin}} - 2}{N_{\text{JK}} - 1} C_{\text{JK}}^{-1}, \quad (57)$$

where the Hartlap factor, $(N_{\text{JK}} - N_{\text{bin}} - 2)/(N_{\text{JK}} - 1)$, accounts for the skewed nature of the inverse Wishart distribution, and N_{bin} is the number of bins. We use 7 k -bins when measuring $\hat{P}_{\text{kSZ}, \ell=1}(k)$ (Sec. 7.2), resulting in a Hartlap factor of 0.96.

In Appendix A, we compare the variances (the diagonal entries of the covariance matrix) of the pairwise

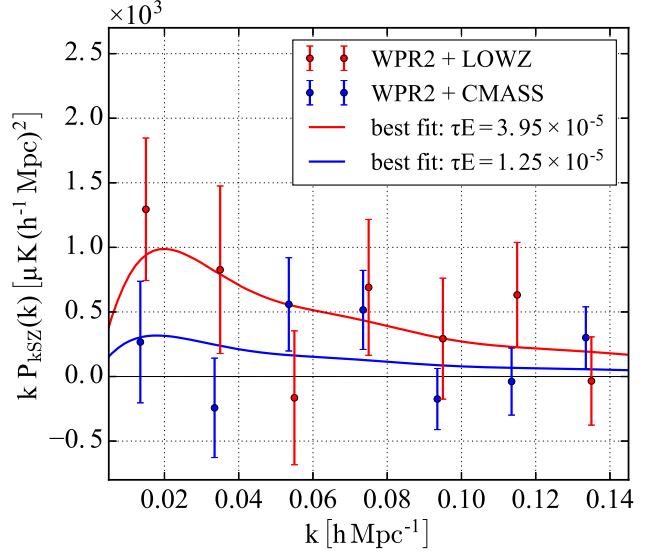


Figure 5. Pairwise kSZ power spectrum dipoles measured from the WPR2 CMB map (Sec. 2.1) with both the LOWZ (red symbols) and CMASS (blue symbols) samples (Sec. 2.2) compared with the best fit models (Sec. 3) including the window function correction (Sec. 5) (red and blue solid lines). The kSZ temperature per each galaxy is estimated using the AP filter with $5'$ ($4'$) aperture radius for the LOWZ (CMASS) sample. The errorbars shown are derived from the 1σ jackknife errors (Sec. 6). Using the fitting range $k = 0.015 - 0.135 h \text{ Mpc}^{-1}$ with 7 separation bins, we find $\tau E = (3.95 \pm 1.62) \times 10^{-5}$ for LOWZ and $\tau E = (1.25 \pm 1.06) \times 10^{-5}$ for CMASS, corresponding to $S/N = 2.44$ and 1.18 , respectively.

kSZ power dipole computed by linear theory developed in Sugiyama et al. (2016a) with those estimated from data itself using the jackknife and bootstrap (Efron 1979) methods for various spatial sub-regions on the sky. There, we find a good agreement between the theory and the data, implying the validities of both our variance model and the variance estimates from data itself.

7 RESULTS

7.1 Fitting prescription

We fit the pairwise kSZ power dipole measured by its estimator in equation (48) with the template given by equation (54) with the optical depth τE being a free parameter. In this paper, we do not analyze the pairwise kSZ correlation function, but we expect similar results to the analysis of the pairwise kSZ power spectrum. Using the covariance matrix derived in Sec. 6, we perform a χ^2 minimization to find the best fitting parameter. Since the optical depth τE is assumed to be a proportionality constant in our template model, the χ^2 minimization procedure provides the estimates for the amplitude of τE and its associated errors as follows:

$$\begin{aligned} \widehat{\tau E} &= \frac{\sum_{i,j} \hat{P}_i C_{ij}^{-1} \hat{P}_j}{\sum_{i,j} \hat{P}_i C_{ij}^{-1} \hat{P}_j}, \\ \Delta(\tau E) &= \left(\sum_{i,j} \hat{P}_i C_{ij}^{-1} \hat{P}_j \right)^{-1/2}, \end{aligned} \quad (58)$$

⁴ https://github.com/esheldon/kmeans_radec/

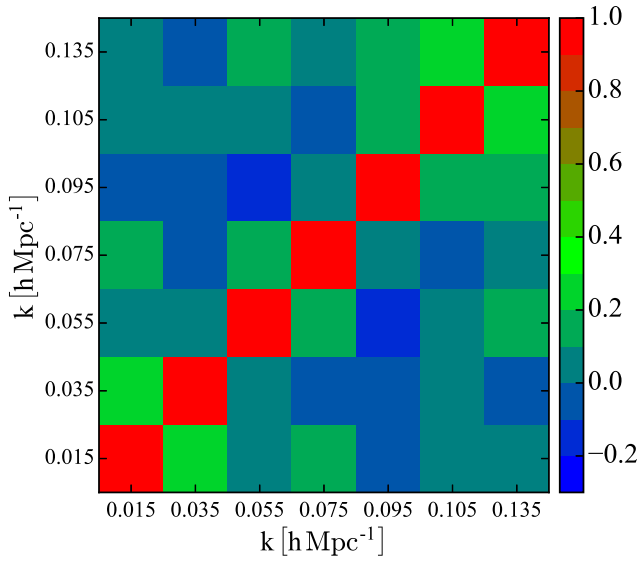


Figure 6. Correlation coefficients of the pairwise kSZ power dipole measured from the WPR2 map with the LOWZ sample using the jackknife method. All the absolute values of the off-diagonal elements are less than 0.25, showing weak correlation between different k -bins.

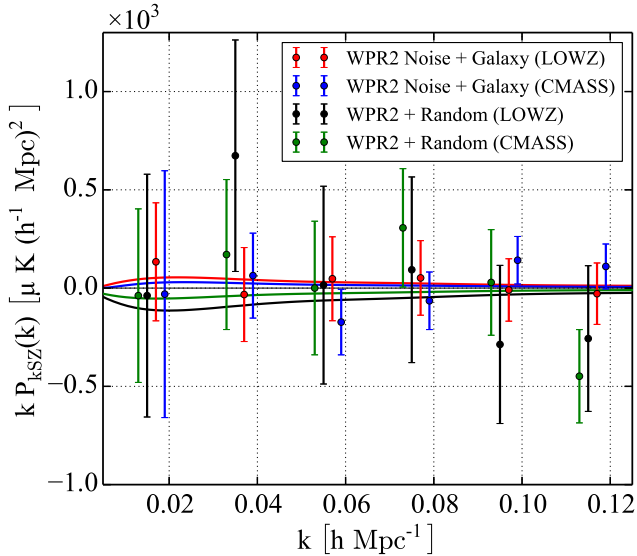


Figure 7. Null tests in the following two ways for both the LOWZ and CMASS samples: the three-dimensional temperature fluctuation, δT in equation (43), is estimated from (1) the WPR2 data map with the random catalogue and from (2) the WPR2 noise map with the galaxy data sample, where the galaxy density fluctuation, δn in equation (43), is estimated from the galaxy data in all four cases. The pairwise kSZ power dipoles and their associated errors shown in this figure are estimated in the same way as Fig. 5. The four solid lines are the best-fitting models for the null tests. In all four cases, the signals are consistent with null hypothesis.

where C_{ij} is the covariance matrix estimated from the observed data itself (equations 55 and 57), \hat{P}_i is the i th k -bin measure of $P_{kSZ, \ell=1}$, and \bar{P}_i is the theoretical template fixing the optical depth to $\tau E = 1$. The statistical significance of the template fit is then computed as $S/N = |\tau E|/\Delta(\tau E)$. In our analysis, we use the full covariance matrix including the off-diagonal elements. We decide to bin the power spectrum in bins of $\Delta k = 0.02 h \text{ Mpc}^{-1}$ and to use the fitting range of $0.015 \leq k \leq 0.135 [h \text{ Mpc}^{-1}]$, thus $N_{\text{bin}} = 7$.

7.2 Pairwise kSZ power spectrum dipole

We present the dipole moment of the pairwise kSZ power spectrum computed using the estimator in equation (48). In Fig. 5, we show our measurements of the dipole from the WPR2 CMB map with the two galaxy samples, LOWZ (red symbols) and CMASS (blue symbols), where the results at the NGC and SGC have been combined into a single measurement (equation 51). Here, the aperture values chosen in this figure are $5'$ for LOWZ and $4'$ for CMASS, which maximize the S/N of the kSZ signal (see Table 1). As expected in Section 3.1.2, the amplitude of the kSZ spectrum for the LOWZ sample is much larger than that for the CMASS sample, as the WPR2 map cannot resolve the CMASS halos.

We estimate the covariance error matrix of the measurement C_{ij} using equations (55) and (57). Fig. 6 displays the correlation coefficient matrix, $r_{ij} = C_{ij}/(C_{ii}C_{jj})^{1/2}$. We observe that the off-diagonal terms of the correlation coefficient are very small and their absolute values are all less than 0.25. For LOWZ, we find the similar coefficient matrix to that for CMASS. The errorbars shown in Fig. 5 are the square root of the diagonal components, $C_{ii}^{1/2}$.

In order to see if the measured signal in Fig. 5 is due to systematic effects, we perform null tests by modifying the three-dimensional temperature fluctuation, δT (equation 43), in two ways for each of the two samples: we estimate δT from (1) the WPR2 data map with the random catalogue and from (2) the WPR2 noise map with the galaxy data sample, where the galaxy density fluctuation, δn (equation 43), is measured from the galaxy data in all four cases. In case 1, we randomly select a subset of the random catalogue, so that the number of objects in the subset matches the real catalogue. By construction these measurements should be equal to zero if there is no systematic effect. The results of these tests are shown in Fig. 7. All four cases are consistent with the expectation of a null signal. We find statistical significances of $S/N = 0.32$ for LOWZ and $S/N = 0.20$ for CMASS in case 1, and of $S/N = 0.33$ for LOWZ and 0.21 for CMASS in case 2. Furthermore, we repeat the null test of case 1 three times by taking different random seeds when selecting a subset of the random catalogue. We have found that all of these tests show $S/N \lesssim 1$ for both LOWZ and CMASS. We conclude from these results that there is no obvious systematic contamination affecting our analysis.

For the aperture values of $5'$ for LOWZ and $4'$ for CMASS, the optical depths τE are respectively constrained to

$$\tau E = (3.95 \pm 1.62) \times 10^{-5}$$

and $\tau E = (1.25 \pm 1.06) \times 10^{-5}$. While for LOWZ, the statistical significance of the kSZ signal is $S/N = 2.44$, for CMASS, the signal is consistent with null hypothesis of no signal,

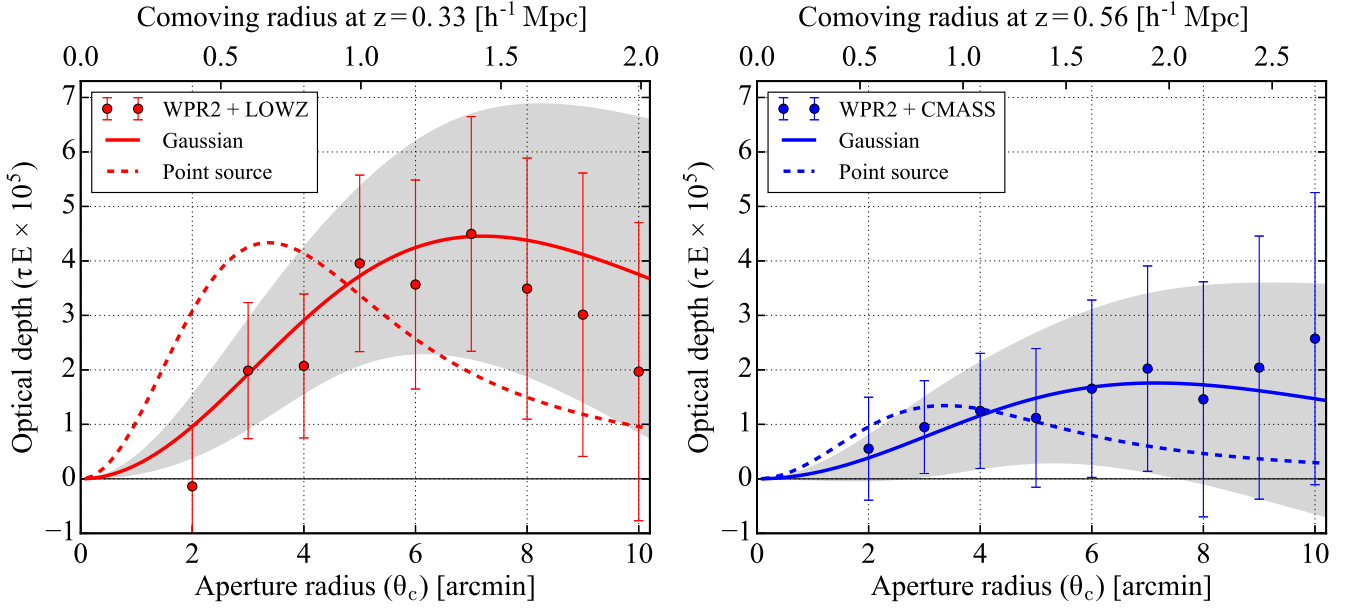


Figure 8. Measured optical depth τE as a function of the angular radius θ_c of the AP filter using the WPR2 map with the LOWZ (left panel) and CMASS (right panel) galaxy samples. The 1σ error bars in this figure are derived from equation (58), and they are highly correlated (see Fig. 9). We compare our measurements with the best fitting models assuming a projected Gaussian gas profile with a characteristic radius σ_R , given by equations (17) and (18) (solid lines). The grey shaded regions are the corresponding 1σ uncertainties computed by linear theory (equation 65). For the LOWZ (CMASS) sample, using the fitting range $\theta_c = 2' - 10'$ ($8'$) with $1'$ bin width, the best fit parameter values are $f_{\text{gas}} = 0.188$ (0.236) and $\sigma_R = 4.02$ (3.98)'. For a comparison, we plot the predictions from the point source model, which corresponds to $\sigma_R = 0$ in the Gaussian model, for $f_{\text{gas}} = 0.04$ (dashed lines). We find a clear shift outward in the peak of the AP filtered optical depth compared to the peak position predicted by the point source assumption.

namely $S/N = 1.18$. The solid lines in figure 5 show the best fit fiducial models given by equation (54).

7.3 Optical depth as a function aperture radii

To measure the optical depth τE as a function of the angular radius of the AP filter θ_c (Sec. 3.1), we repeat the analysis of the pairwise kSZ power performed in the previous subsection for various aperture radii. We summarize the resulting best-fitting values of the optical depth τE with their 1σ errors in Table 1. This analysis is similar to that used in Schaan et al. (2016), while the authors in Schaan et al. (2016) have measured the kSZ signal by stacking the CMB temperature at the location of each halo.

Fig. 8 shows our measurements of the optical depth $\tau E(\theta_c)$ from the WPR2 CMB map with the two galaxy samples, LOWZ (left panel) and CMASS (right panel). The best fit curves are obtained by the Gaussian gas profile model (solid lines). As expected in Sec. 3.1, especially for LOWZ, we find that the peak position of the AP filtered optical depth clearly shifts outward compared to that predicted by the point source assumption (dashed lines). The peak position is estimated as $\theta_{\text{peak}} = 2^{3/4} \sqrt{\sigma_B^2 + \sigma_R^2} = 7.63'$ for LOWZ and $7.57'$ for CMASS (equation 21).

The measurements of τE for different θ_c are strongly correlated, because the data for a smaller θ_c is a subset of the data for a larger θ_c . To estimate the covariance matrix of the AP filtered optical depth, we rewrite the optical depth

estimator (equation 58) as a function of θ_c :

$$\widehat{\tau E}(\theta_c) = \frac{\sum_{i,j} \widehat{P}_i(\theta_c) C_{ij}^{-1}(\theta_c) \bar{P}_j}{\sum_{i,j} \bar{P}_i C_{ij}^{-1}(\theta_c) \bar{P}_j}, \quad (59)$$

where the pairwise kSZ power dipole $\widehat{P}_i(\theta_c)$ and its covariance matrix $C_{ij}(\theta_c)$ are measured from the AP filtered CMB map with the aperture radius being θ_c , and \bar{P} is the theoretical template fixing the optical depth to $\tau E = 1$. Then, the covariance of $\widehat{\tau E}(\theta_c)$ is given by

$$\begin{aligned} \text{Cov} \left(\widehat{\tau E}(\theta_a), \widehat{\tau E}(\theta_b) \right) &= \sum_{i,j} \sum_{k,l} \text{Cov} \left(\widehat{P}_i(\theta_a), \widehat{P}_k(\theta_b) \right) \\ &\times \frac{C_{ij}^{-1}(\theta_a) \bar{P}_j}{\left(\sum_{k,j} \bar{P}_i C_{ij}^{-1}(\theta_a) \bar{P}_j \right)} \\ &\times \frac{C_{kl}^{-1}(\theta_b) \bar{P}_l}{\left(\sum_{i,j} \bar{P}_i C_{ij}^{-1}(\theta_b) \bar{P}_j \right)}, \quad (60) \end{aligned}$$

where θ_a, θ_b [arcmin] = {2, 3, 4, 5, 6, 7, 8, 9, 10}, and $\text{Cov} \left(\widehat{P}_i(\theta_a), \widehat{P}_k(\theta_b) \right)$ is the covariance of $P_{\text{kSZ}, \ell=1}$ between two different aperture radii, which is estimated from equation (55) by replacing the variable y_i^k by a function of the aperture radius $y_i^k(\theta)$. The square root of the diagonal elements of the covariance, $\text{Cov}^{1/2} \left(\widehat{\tau E}(\theta), \widehat{\tau E}(\theta) \right)$ for $\theta_a = \theta_b$, reproduces the error on the optical depth at a fixed θ_c , $\Delta(\tau E)$ (equation 58).

Fig. 9 displays the correlation coefficient matrix for different aperture radii measured from the WPR2 map with the LOWZ sample. As expected, off-diagonal terms of the covariance present strong correlation, especially for the largest

| AP filter θ_c [arcmin] | τE [10^{-5}] | $\Delta(\tau E)$ [10^{-5}] | S/N |
|-------------------------------|------------------------|--------------------------------|------|
| WPR2 + LOWZ | | | |
| $\theta_c = 2$ | -0.14 | 1.12 | 0.13 |
| $\theta_c = 3$ | 1.99 | 1.25 | 1.59 |
| $\theta_c = 4$ | 2.07 | 1.32 | 1.57 |
| $\theta_c = 5$ | 3.95 | 1.62 | 2.44 |
| $\theta_c = 6$ | 3.57 | 1.92 | 1.86 |
| $\theta_c = 7$ | 4.50 | 2.15 | 2.09 |
| $\theta_c = 8$ | 3.50 | 2.40 | 1.46 |
| $\theta_c = 9$ | 3.01 | 2.60 | 1.16 |
| $\theta_c = 10$ | 1.97 | 2.73 | 0.72 |
| WPR2 + CMASS | | | |
| $\theta_c = 2$ | 0.55 | 0.94 | 0.59 |
| $\theta_c = 3$ | 0.95 | 0.85 | 1.12 |
| $\theta_c = 4$ | 1.25 | 1.06 | 1.18 |
| $\theta_c = 5$ | 1.12 | 1.27 | 0.88 |
| $\theta_c = 6$ | 1.65 | 1.63 | 1.01 |
| $\theta_c = 7$ | 2.02 | 1.88 | 1.07 |
| $\theta_c = 8$ | 1.46 | 2.16 | 0.68 |
| $\theta_c = 9$ | 2.04 | 2.41 | 0.85 |
| $\theta_c = 10$ | 2.57 | 2.68 | 0.96 |

Table 1. Best-fit values of the measured optical depth with their associated 1σ errors for various aperture radii. The statistical significance for each aperture radius is estimated as $S/N = |\tau E|/\Delta(\tau E)$.

apertures. We have confirmed the similar results also for CMASS. The 1σ errorbars shown in Fig. 8 are the square root of the diagonal elements of the covariance matrix, which are derived from equation (58). The errors increase with increasing AP filter radius θ_c , because contamination from primary CMB anisotropies increases for larger aperture radii. The grey shaded regions in Fig. 8 are the corresponding 1σ uncertainties computed using linear theory developed in this work (see Sec. 8 and Appendix A), which are consistent with the errorbars estimated from the data itself.

In our analysis, we adopt the optical depth model assuming the projected Gaussian gas profile with a characteristic radius σ_R (equations 17 and 18). We fit the measured optical depth $\tau E(\theta)$ with the template given by equation (17) with the gas fraction f_{gas} and the radius σ_R being two free parameters. The gas fraction f_{gas} is proportional to the kSZ signal; the radius σ_R characterizes how far a gas cloud can spread over a halo. In the Gaussian profile, the limit of $\sigma_R = 0$ corresponds to the assumption that observed galaxies can be treated as point sources. We do not perform analyses for other gas profiles in this work, because the errors on τE are too large to determine the shape of detailed gas profiles, e.g. slope β and core radius θ_R in the β -profile given by equation (18).

We determine the best fitting values of f_{gas} and σ_R by minimizing

$$\chi^2 = \sum_{a,b} [\widehat{\tau E}(\theta_a) - \tau E^{\text{model}}(\theta_a)] C_{ab}^{-1} [\widehat{\tau E}(\theta_b) - \tau E^{\text{model}}(\theta_b)], \quad (61)$$

where C_{ab} is the covariance matrix of τE given by equation (60). We use the fitting range $\theta_c = 2'-10'$ for LOWZ and $\theta_c = 2'-8'$ for CMASS with $\Delta\theta_c = 1'$, corresponding to 9 and 7 separation bins, respectively. We then find

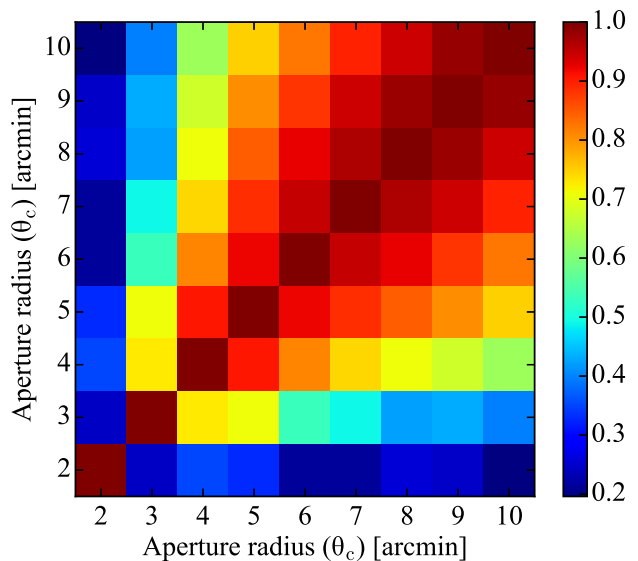


Figure 9. Correlation coefficients of the optical depth for different aperture radii measured from the WPR2 map with the LOWZ sample. The covariance of the AP filtered optical depth presents strong correlation between different data points, especially for the largest apertures.

$(f_{\text{gas}}, \sigma_R) = (0.188, 4.02')$ for LOWZ and $(0.236, 3.98')$ for CMASS.

By computing the χ^2 statistics for the optical depth in equation (61) with the two varying parameters f_{gas} and σ_R , we present the constraints on f_{gas} and σ_R from the WPR2 map with LOWZ, and show the result in Fig. 10. For CMASS, statistical uncertainties are too large to constrain on these parameters; therefore, we focus only on LOWZ. Since the amplitude of the optical depth decreases with increasing σ_R , there is a strong degeneracy between f_{gas} and σ_R . The best fit value of the gas fraction, $f_{\text{gas}} = 0.188$, is consistent with the universal baryon fraction $\Omega_b/\Omega_m = 0.155$ within the 1σ contour. The best fit value of the characteristic radius, $\sigma_R = 4.0'$, is slightly larger than the virial radius of the LOWZ halos, $R_{200}/D_A = 2.7'$, beyond the 1σ level but is still consistent with the virial radius within the 2σ level. We calculate the χ^2 statistics in equation (61) divided by degrees of freedom (d.o.f.) with respect to the best fit value ($\chi_{\text{min}}^2/\text{d.o.f.}$); we find $\chi_{\text{min}}^2/\text{d.o.f.} = 10.6/7$. We calculate $\Delta\chi^2 = \chi^2 - \chi_{\text{min}}^2 = 6.54$ for the point source assumption ($\sigma_R = 0$). This corresponds to a probability to exceed (PTE) of 3.8% or, assuming Gaussian uncertainties, a rejection of the point source assumption at the 2.1σ level.

8 FORECASTS FOR FUTURE SURVEYS

We conduct a Fisher matrix analysis (see Tegmark et al. (1997) for a review) to see how the next generation of high-resolution CMB experiments can improve constraints on parameters in the optical depth model (equation 17). To estimate a realistic forecast for parameter constraints for a given survey, it is essential to quantify statistical errors on the observables of interest, the pairwise kSZ dipole $P_{\text{kSZ}, \ell=1}(k)$ and the optical depth $\tau E(\theta)$. In this section, we present the theoretical prediction of the covariance matrix of τE , which

| FWHM [arcmin] | noise [μK -arcmin] | galaxy | redshift | V [[h^{-1} Gpc) 3] | \bar{n}_g [[h^{-1} Mpc) $^{-3}$] | b_g | M_{halo} [[h^{-1} M_{\odot}] | S/N (FWHM = 1', 1.5', 2.0', 3.0') |
|------------------|-----------------------------|--------|-------------------------|--------------------------------|---|-------|--|--------------------------------------|
| CMB-S4 + BOSS | | | | | | | | |
| 1 – 3 | 2 | LRG | 0.3 (0.15 < z < 0.43) | 2.0 | 3.0×10^{-4} | 2.0 | 5.2×10^{13} | (13, 12, 12, 12) |
| 1 – 3 | 2 | LRG | 0.5 (0.43 < z < 0.70) | 4.0 | 3.0×10^{-4} | 2.0 | 2.6×10^{13} | (46, 43, 39, 32) |
| CMB-S4 + DESI | | | | | | | | |
| 1 – 3 | 2 | LRG | 0.8 (0.65 < z < 0.95) | 13.5 | 2.8×10^{-4} | 2.5 | 5.0×10^{13} | (105, 98, 90, 75) |
| 1 – 3 | 2 | ELG | 1.1 (0.95 < z < 1.25) | 18.7 | 4.7×10^{-4} | 1.4 | 4.0×10^{12} | (92, 69, 52, 28) |
| CMB-S4 + PFS | | | | | | | | |
| 1 – 3 | 2 | ELG | 0.9 (0.6 < z < 1.2) | 2.3 | 4.9×10^{-4} | 1.3 | 4.0×10^{12} | (34, 27, 21, 12) |
| 1 – 3 | 2 | ELG | 1.5 (1.2 < z < 2.0) | 4.9 | 4.7×10^{-4} | 1.7 | 5.0×10^{12} | (54, 39, 30, 16) |

Table 2. Assumed experimental parameters for forecasts. The first two columns show beam size and detector noise in a CMB-S4-type CMB experiment. Since the parameters of CMB-S4 are not yet fixed, we assume a range of beam sizes from 1' to 3'. From the third to eighth columns show type of galaxies (LRGs or ELGs), redshift z , comoving survey volume V , mean comoving number density \bar{n}_g , linear bias parameter b_g , and mean halo mass M_{halo} . The last column presents the signal-to-noise ratios of the kSZ signal for some of the beam sizes (see also Fig. 11). The rows denote different three spectroscopic galaxy surveys, BOSS-, DESI-, and PFS-like surveys in two redshift bins.

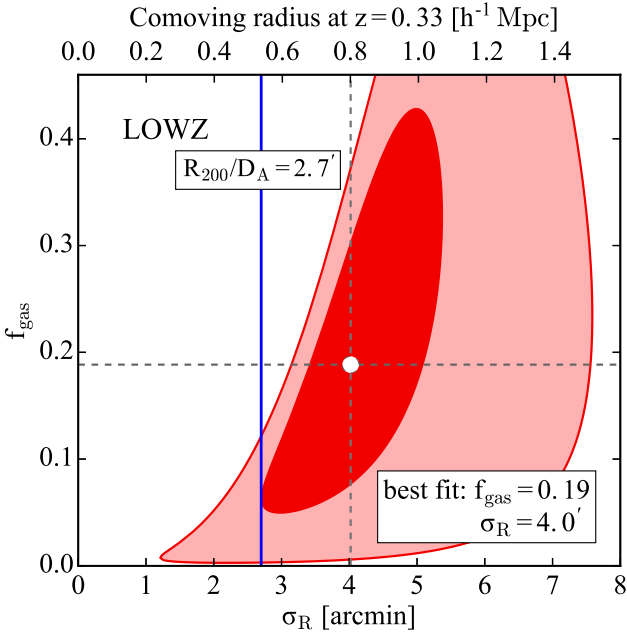


Figure 10. Constraint on f_{gas} and σ_R for the LOWZ halos. The contours show the $\Delta\chi^2 = 2.30$ (68.3% CL) and $\Delta\chi^2 = 6.17$ (95.4% CL). The blue line means the virial radius R_{200}/D_A . The best-fit value of the gas fraction, $f_{\text{gas}} = 0.188$, is consistent with the universal baryon fraction $\Omega_b/\Omega_m = 0.155$ within the 1σ contour, and the best-fit value of the characteristic radius, $\sigma_R = 4.0'$, is consistent with the virial radius for the LOWZ halos within the 2σ contour. The point source assumption that corresponds to $\sigma_R = 0$ is ruled out at the 2.1σ level.

is derived from the covariance matrix of $P_{\text{kSZ}, \ell=1}$, and perform the Fisher analysis for τE using it. We describe the full deviation of the covariance matrix of $P_{\text{kSZ}, \ell=1}$ in Appendix A and restrict the discussion here to the main results. The results we obtain depend upon a fiducial model and assumed survey parameters.

For a data vector that is predictable given parameters

p_α , the Fisher information matrix is:

$$F_{\alpha\beta} = - \left\langle \frac{\partial^2 \ln L}{\partial p_\alpha \partial p_\beta} \right\rangle, \quad (62)$$

where L is the likelihood function of the data set given the fiducial parameters p_1, \dots, p_α . The partial derivative with respect to parameter p_α is evaluated around the fiducial model. In the limit of Gaussian likelihood surface, the Cramer-Rao inequality shows that the Fisher matrix quantifies the best statistical errors achievable on parameter determination, marginalized over all the other parameters: $\Delta p_\alpha \geq (F^{-1})_{\alpha\alpha}^{1/2}$, where (F^{-1}) denotes the inverse of the Fisher matrix, and Δp_α is the relative error on p_α around its fiducial value.

Before computing the fisher matrix for the optical depth, we need to compute the covariance matrix of the pairwise kSZ dipole, which is given by equation (A3) in linear theory:

$$\text{Cov} \left(\hat{P}_{\text{kSZ}, \ell=1}(k_1; \theta_a), \hat{P}_{\text{kSZ}, \ell=1}^*(k_2; \theta_b) \right) = \frac{\delta_{k_1 k_2}^{\text{K}}}{N_{\text{mode}}(k_1)} C_{\text{kSZ}}(k_1; \theta_a, \theta_b), \quad (63)$$

where $\hat{P}_{\text{kSZ}, \ell=1}(k; \theta)$ is the pairwise kSZ power dipole estimated for a AP filter radius θ , $N_{\text{mode}}(k) = 4\pi k^2 \Delta k V / (2\pi)^3$ is the number of independent Fourier modes in a bin with Δk and V being bin width and a given survey volume respectively, and δ^{K} denotes the Kronecker delta such that $\delta_{k_1 k_2}^{\text{K}} = 1$ if $k_1 = k_2$ within the bin width, otherwise zero. The function $C_{\text{kSZ}}(k; \theta_a, \theta_b)$ is given by equation (A8), which depends on the model of the optical depth (equation 17) and the root-mean-square (rms) of the AP filtered CMB maps (equation A5)

$$\sigma_N^2(\theta_a, \theta_b) = \sum_{\ell}^{\ell_{\text{max}}} \frac{2\ell + 1}{4\pi} \langle C_{\ell}^{\text{obs}} \rangle U(\ell\theta_a) U(\ell\theta_b), \quad (64)$$

where C_{ℓ}^{obs} is the observed CMB angular power spectrum, and $U(\ell\theta)$ is the AP filter function (equation 11). The ensemble average of C_{ℓ}^{obs} is predictable from $\langle C_{\ell}^{\text{obs}} \rangle = B_{\ell}^2 C_{\ell}^{\text{the}} + N_{\ell}$, where C_{ℓ}^{the} is the theoretical prediction of the CMB power spectrum, $B_{\ell} = e^{-\sigma_B^2 \ell^2 / 2}$ is the Gaussian beam function, and N_{ℓ} denotes detector noise.

Substituting equation (63) into equation (60), we obtain

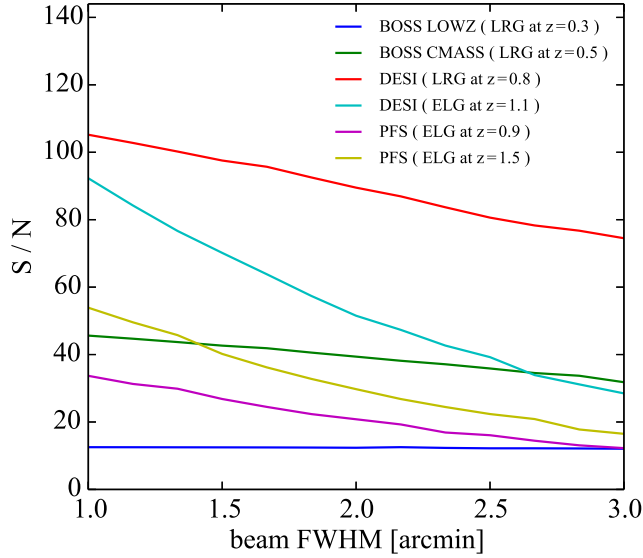


Figure 11. Signal-to-noise ratios of the optical depth as a function of beam sizes for a CMB-S4-type CMB experiment with BOSS-, DESI-, and PFS-like spectroscopic galaxy surveys (For details, see Table 2). We forecast that the DESI surveys for two types of galaxies, LRGs and ELGs, achieve $S/N \sim 100$ for $\text{FWHM} = 1'$. Since the signal of the ELGs is on scales smaller than several arc minutes, the S/N for the ELG surveys increases with improving experimental resolution.

the analytic form of the covariance matrix of the optical depth

$$\text{Cov}(\widehat{\tau E}(\theta_a), \widehat{\tau E}(\theta_b)) = \frac{1}{V} \frac{M(\theta_a, \theta_b)}{N(\theta_a)N(\theta_b)}, \quad (65)$$

where

$$\begin{aligned} M(\theta_a, \theta_b) &= \int_{k_{\min}}^{k_{\max}} \frac{d^3 k}{(2\pi)^3} \frac{C_{\text{kSZ}}(k; \theta_a, \theta_b) [\bar{P}(k)]^2}{C_{\text{kSZ}}(k; \theta_a, \theta_a) C_{\text{kSZ}}(k; \theta_b, \theta_b)} \\ N(\theta_a) &= \int_{k_{\min}}^{k_{\max}} \frac{d^3 k}{(2\pi)^3} \frac{[\bar{P}(k)]^2}{C_{\text{kSZ}}(k; \theta_a, \theta_a)} \end{aligned} \quad (66)$$

with $\bar{P}(k)$ being $P_{\text{kSZ}, \ell=1}(k)$ computed for $\tau E = 1$. We note that the covariance matrix of τE does not depend on the binning of both the pairwise kSZ power spectrum and the optical depth. For the calculation of τE for observational data, it is therefore best to choose very small bin widths, in order to minimize discretization errors. As shown in Appendix A, the rms σ_N^2 appears in the covariance matrix of $P_{\text{kSZ}, \ell=1}$ with the shot-noise term $1/\bar{n}_g$, where \bar{n}_g is the mean comoving number density of galaxies, so that higher values of the mean number density yield lower errors on τE . Furthermore, since the covariance scales as $1/V$ in equation (65), larger volume surveys are suitable for the measurements of the optical depth via the kSZ effect.

Finally, we derive the Fisher matrix for the optical depth

$$F_{\alpha\beta} = \sum_{a,b} \frac{\partial \tau E(\theta_a)}{\partial p_\alpha} \text{Cov}^{-1}(\widehat{\tau E}(\theta_a), \widehat{\tau E}(\theta_b)) \frac{\partial \tau E(\theta_b)}{\partial p_\beta}, \quad (67)$$

where we assumed that the covariance matrix of the optical depth is independent of the parameters p_α , because we expect that the parameter dependence of the covariance becomes a sub-dominant part of the likelihood function once

the parameters are sufficiently precisely determined. In what follows, we use the currently concordant flat Λ CDM model (Sec. 1). For a fair comparison with our measurements in the previous section (Fig. 8 and 10), we adopt the model of the optical depth given by equation (17), which assumes a projected Gaussian gas profile with a characteristic radius estimated by the virial radius, $\sigma_R = R_{200}/D_A$; we assume that the gas fraction is the same as the universal baryon fraction $f_{\text{gas}} = \Omega_b/\Omega_m = 0.155$. We then allow the same two parameters to vary as those used as the fitting parameters in our analysis: $p_\alpha = \{f_{\text{gas}}, \sigma_R\}$. We also calculate the expected signal-to-noise (S/N) ratio for τE ,

$$\left(\frac{S}{N}\right)^2 = \sum_{a,b} \tau E(\theta_a) \text{Cov}^{-1}(\widehat{\tau E}(\theta_a), \widehat{\tau E}(\theta_b)) \tau E(\theta_b), \quad (68)$$

where the inverse of the S/N estimates the uncertainty of the gas fraction f_{gas} when all the other parameters are fixed: $\Delta f_{\text{gas}}/f_{\text{gas}} = (S/N)^{-1}$.

Estimating errors on the optical depth, we ignore the contribution from the pairwise kSZ octopole, as the S/N of the octopole is about ten times smaller than that of the dipole. The octopole can be used to break the degeneracy among the optical depth, the growth rate and the linear bias in the pairwise kSZ signal when we vary all these parameters (Sugiyama et al. 2016a). However, including the octopole improves the constraint on the optical depth at only a few percent level in our analysis that we fix all the other parameters.

We specify survey parameters that well resemble a CMB-S4-type CMB experiment with BOSS-, DESI-, and PFS-like spectroscopic galaxy surveys in Table 2. Since the parameters of CMB-S4 are not yet fixed, we assume a range of beam sizes from $1'$ to $3'$ with detector noise of $2 \mu\text{K}$ -arcmin. Here, we consider two types of galaxies, luminous red galaxies (LRGs) and [OII] emission line galaxies (ELGs). On the one hand, LRGs lie in massive halos with $\sim 10^{13} h^{-1} M_\odot$ and are a potentially-useful tracer of large-scale structure for the kSZ measurement. On the other hand, ELGs are particularly useful tracers to probe baryons via the kSZ effect out to even higher redshift ($z \gtrsim 1.0$) and lower halo mass ($\sim 10^{12} h^{-1} M_\odot$), a range of redshift and mass that is difficult to probe baryons except for the kSZ measurement. We assume that fiducial biases b_g follow constant $b_g(z)D(z)$, where $D(z)$ is the linear growth function. For LRGs and ELGs, we use $b_{\text{LRG}}D(z) = 1.7$ and $b_{\text{ELG}}D(z) = 0.84$, respectively (Mostek et al. 2013; DESI Collaboration et al. 2016). We estimate mean halo mass from the assumed bias using Press-Schechter theory (Press & Schechter 1974) with Sheth-Tormen mass function (Sheth & Tormen 1999). Computing the Fisher matrix and S/N for τE , we choose $\ell_{\max} = \pi/\sigma_B$ in equation (64), $k_{\min} = 0.01 h \text{Mpc}^{-1}$ and $k_{\max} = 0.2 h \text{Mpc}^{-1}$ in equation (65); we adopt ranges of the AP filter of $\theta_c = 0.5' - 7'$ for LRGs and $\theta_c = 0.5' - 3'$ for ELGs with 20 separation bins.

We ignore contamination from the tSZ effect in equation (64), because multiple frequency data in a CMB-S4 like experiment can be used to remove other foregrounds including the tSZ effect. The tSZ cleaning may increase the noise levels significantly beyond the $2 \mu\text{K}$ -arcmin that we use in our analysis. We further ignore the other frequency-dependent components such as CIB, which will become dom-

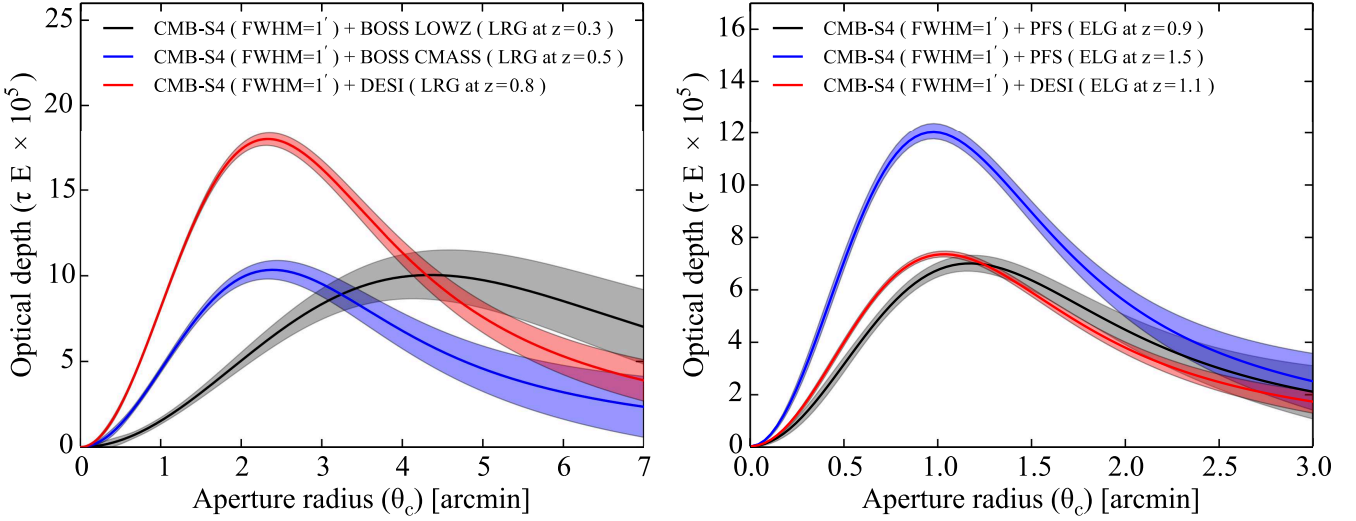


Figure 12. Theoretical predictions for the optical depth as a function of the angular radius θ_c of the AP filter, where the resolution of an assumed CMB experiment is $\text{FWHM} = 1'$. The theoretical predictions of the optical depth (solid coloured lines) are given by equation (17), which assumes a projected Gaussian gas profile, and their 1σ errors (coloured regions) are the standard deviations computed by equation (65) in linear perturbation theory. We show the predictions of the optical depth for two types of galaxies, LRGs and ELGs, in the left panel and the right panel, respectively. A remarkable difference between LRGs and ELGs is the mass of halos hosting these galaxies: $M \sim 10^{13} M_\odot$ for LRGs and $M \sim 10^{12} M_\odot$ for ELGs. In the left panel, the predictions for LOWZ (black regions) and CMASS (blue regions) can be compared to the left and right panels in Fig. 8, respectively.

inant contribution to the expected errors on the kSZ signal for a high resolution CMB experiment. We expect that these contaminations would make the expected S/N of the kSZ signal in this analysis smaller. A more detail analysis is left for future works.

Fig. 11 shows the S/N of the optical depth as a function of beam sizes. In the last column of Table 2, we present the values of the S/N for some of the CMB beam sizes, $\text{FWHM} = 1', 1.5', 2.0', \text{ and } 3.0'$. As expected, the LRG survey in DESI can achieve higher S/N than the ELG survey in DESI, as the mean halo mass for LRGs is higher than that for ELGs. However, the difference between halo masses of LRGs and ELGs, $\sim 10^{13} M_\odot$ and $\sim 10^{12} M_\odot$, does not become significant when CMB experiments have a sufficient resolution to resolve the host halos of a given galaxy sample, because the kSZ signal is then proportional to $M^{1/3}$ as shown in Section 3.1.2. In fact, the expected S/Ns for LRGs and ELGs in DESI are ~ 100 in both types of galaxies for $\text{FWHM} = 1'$. Thus, the S/Ns for the ELG surveys of DESI and PFS significantly increase with decreasing beam sizes. On the other hand, the S/N for LOWZ becomes flat in a range from $\text{FWHM} = 1'$ to $3'$, because the LOWZ halos are already resolved for $\text{FWHM} = 3'$.

Fig. 12 shows the theoretical predictions for the optical depth as a function of the AP filter radius θ_c , which are given by equation (17). The shaded regions are the 1σ uncertainties that are the standard deviations computed by equation (65). To compute the predictions of the optical depth and their errors, we assume a CMB-S4 like experiment with the resolution of $\text{FWHM} = 1'$ and three spectroscopic galaxy surveys described in Table 2. The left and right panels show the predictions for two types of galaxies, LRGs and ELGs, respectively.

In Fig. 13, we show the forecast constraints on f_{gas} and σ_R that are derived from the expected survey param-

eters of CMB-S4 with $\text{FWHM} = 1'$ and BOSS, DESI, and PFS in two redshift bins (Table 2). In the $f_{\text{gas}} - \sigma_R$ plane, the marginalized 1σ errors on f_{gas} and σ_R are $(\Delta f_{\text{gas}}/f_{\text{gas}}, \Delta \sigma_R/\sigma_R) = (2.1\%, 0.5\%)$ for DESI at $z = 0.8$ (purple), $(4.8\%, 1.2\%)$ for BOSS CMASS at $z = 0.5$ (yellow), $(16.6\%, 3.2\%)$ for BOSS LOWZ at $z = 0.3$ (orange), $(1.7\%, 1.3\%)$ for DESI at $z = 1.1$ (red), $(2.9\%, 2.3\%)$ for PFS at $z = 1.5$ (blue), and $(5.1\%, 2.8\%)$ for PFS at $z = 0.9$ (black).

9 CONCLUSIONS

We have presented the first measurement of the pairwise kSZ power spectrum by combining the WPR2 CMB map, which jointly uses both Planck and WMAP9 data, with the CMASS and LOWZ galaxy samples derived from BOSS DR12. We apply an aperture photometry filter to estimate the CMB temperature distortion associated with each galaxy and measure the filtered optical depth of the host halos of a given galaxy sample via the pairwise kSZ signal. By repeating the analyses of the pairwise kSZ power in the filtered CMB maps for various aperture radii, we measure the optical depth as a function of the aperture radius and constrain the gas fraction, f_{gas} , as well as a parameter of an assumed Gaussian gas profile, the characteristic radius σ_R . This analysis is a direct measurement of baryonic matter in the Universe that is insensitive to the gas temperature. While the S/N of the current measurement is low, this paper both illustrates the methodology for future surveys and places constraints on the optical depth.

Table 1 summarizes our constraints on the optical depth for various aperture radii, and Fig. 8 plots them. In our analysis, we constrain not the optical depth τ itself but the product τE , where $E = H/H_0$ is the ratio between the Hubble

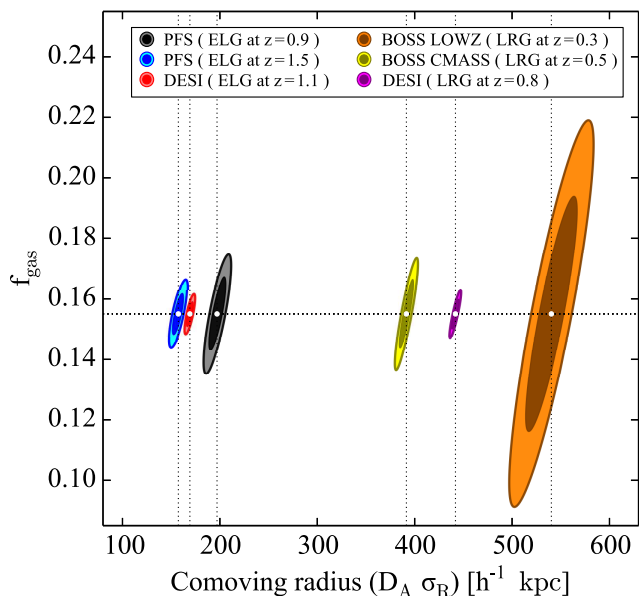


Figure 13. Forecast confidence contours (1- and 2- σ coloured ellipses) placed on f_{gas} and σ_{R} derived from our Fisher matrix analysis, assuming the survey parameters of CMB-S4 with FWHM = 1' and the three galaxy surveys, BOSS, DESI, and PFS, in two redshift bins. For display purposes, we plot $D_{\text{A}}\sigma_{\text{R}}$ on the x-axis, though the varying parameter is σ_{R} . For DESI at $z = 0.8$ (purple regions), the marginalized 1- σ errors on f_{gas} and σ_{R} are $(\Delta f_{\text{gas}}/f_{\text{gas}}, \Delta\sigma_{\text{R}}/\sigma_{\text{R}}) = (2.1\%, 0.5\%)$. For the other surveys, see text. The prediction for LOWZ (orange regions) can be compared to Fig. 10.

parameters at redshift z and the present day. For LOWZ, we find $\tau E = (3.95 \pm 1.62) \times 10^{-5}$ for 5' aperture, corresponding to a statistical significance of $S/N = 2.44$. For CMASS, the kSZ signal is consistent with null hypothesis of no signal. Fig. 10 shows the degeneracy between the gas fraction and the characteristic radius of the Gaussian gas profile with their best fitting values, $(f_{\text{gas}}, \sigma_{\text{R}}) = (0.19, 4.0')$, for LOWZ. This result implies that the gas fraction is consistent with the universal baryon fraction $f_{\text{b}} = \Omega_{\text{b}}/\Omega_{\text{m}} = 0.155$ within the 1 σ level, and that the gas radius, which is roughly estimated by $\sigma_{\text{R}}D_{\text{A}}$ with the angular diameter distance D_{A} , is consistent with the virial radius R_{200} within the 2 σ level. The point source assumption in the model of the gas profile is ruled out at the 2.1 σ level for the LOWZ halos, implying the presence of the spread of the free electron gas in the LOWZ halos. While we have analyzed the projected Gaussian gas profile in this paper, we defer a more detailed study of gas profile models for future kSZ works (e.g., Flender et al. (2016a)).

To illustrate the constraining power of the kSZ measurement on the optical depth, we provide a forecast of future kSZ measurements by performing the Fisher analysis. For the computation of the Fisher matrix, we assume a CMB-S4-type CMB experiment with BOSS-, DESI-, and PFS-like spectroscopic galaxy surveys. These galaxy surveys measure two types of galaxies, LRGs and ELGs, which lies in halos with masses of $\sim 10^{13} M_{\odot}$ and $\sim 10^{12} M_{\odot}$ and at redshifts of $z \lesssim 1.0$ and $z \gtrsim 1.0$, respectively. Thus, the future measurements of the kSZ signal for various galaxy surveys will allow one to constrain the properties

of the free electron gas within halos for a broad range of mass and redshift. In particular, both the LRG and ELG surveys in DESI will achieve detections of the kSZ signal with $S/N \sim 100$ for CMB-S4 assuming FWHM = 1'. This forecast strengthens the motivation for CMB-S4 making small scale measurement of CMB temperature fluctuations over regions of the sky covered by upcoming redshift surveys. While this paper emphasized the upcoming the CMB-S4 experiment and the DESI and PFS surveys, we anticipate that we would reach similar conclusions for the CMB experiment of Advanced ACTPol (Calabrese et al. 2014; Henderson et al. 2016) and the spectroscopic surveys of the ESA satellite mission Euclid (Laureijs et al. 2011; Amendola et al. 2016) and NASA's Wide Field Infrared Survey Telescope (WFIRST; Spergel et al. (2013)).

ACKNOWLEDGEMENTS

We are grateful to Chiaki Hikage, Maresuke Shiraishi, Akito Kusaka, Shun Saito, Hironao Miyatake, Masamune Oguri, Daisuke Nagai, Masato Shirasaki, and Eiichiro Komatsu for very useful discussion. NSS acknowledges financial support from Grant-in-Aid for JSPS Fellows (No. 28-1890). NSS further acknowledges financial support from Grant-in-Aid for Scientific Research from the JSPS Promotion of Science (25287050) and from a NEXT project ‘‘Priority issue 9 to be tackled by using post-K computer’’. The Flatiron Institute is supported by the Simons Foundation. Numerical computations were carried out on Cray XC30 at Center for Computational Astrophysics, National Astronomical Observatory of Japan. We thank the LGMCA team for publicly releasing their CMB maps. Some of the results in this paper have been derived using the *HEALPix* package (Górski et al. 2005). Linear matter power spectra and CMB temperature power spectra used in this paper are generated with *CLASS* (Lesgourgues 2011).

Funding for SDSS-III has been provided by the Alfred P. Sloan Foundation, the Participating Institutions, the National Science Foundation, and the U.S. Department of Energy Office of Science. The SDSS-III web site is <http://www.sdss3.org/>. SDSS-III is managed by the Astrophysical Research Consortium for the Participating Institutions of the SDSS-III Collaboration including the University of Arizona, the Brazilian Participation Group, Brookhaven National Laboratory, Carnegie Mellon University, University of Florida, the French Participation Group, the German Participation Group, Harvard University, the Instituto de Astrofísica de Canarias, the Michigan State/Notre Dame/JINA Participation Group, Johns Hopkins University, Lawrence Berkeley National Laboratory, Max Planck Institute for Astrophysics, Max Planck Institute for Extraterrestrial Physics, New Mexico State University, New York University, Ohio State University, Pennsylvania State University, University of Portsmouth, Princeton University, the Spanish Participation Group, University of Tokyo, University of Utah, Vanderbilt University, University of Virginia, University of Washington, and Yale University.

Based on observations obtained with Planck (<http://www.esa.int/Planck>), an ESA science mission with instruments and contributions directly funded by ESA Member States, NASA, and Canada.

REFERENCES

- Abazajian K. N., et al., 2009, *ApJS*, **182**, 543
- Abazajian K. N., et al., 2015, *Astroparticle Physics*, **63**, 55
- Alam S., et al., 2015, *ApJS*, **219**, 12
- Alam S., et al., 2016, preprint, ([arXiv:1607.03155](https://arxiv.org/abs/1607.03155))
- Alcock C., Paczynski B., 1979, *Nature*, **281**, 358
- Alonso D., Louis T., Bull P., Ferreira P. G., 2016, *Phys. Rev. D*, **94**, 043522
- Amendola L., et al., 2016, preprint, ([arXiv:1606.00180](https://arxiv.org/abs/1606.00180))
- Anderson L., et al., 2014, *MNRAS*, **441**, 24
- Battaglia N., 2016, *J. Cosmology Astropart. Phys.*, **8**, 058
- Baumann D., Nicolis A., Senatore L., Zaldarriaga M., 2012, *J. Cosmology Astropart. Phys.*, **7**, 051
- Bennett C. L., et al., 2013, *ApJS*, **208**, 20
- Bernardeau F., Colombi S., Gaztañaga E., Scoccimarro R., 2002, *Phys. Rep.*, **367**, 1
- Beutler F., et al., 2014, *MNRAS*, **443**, 1065
- Beutler F., et al., 2016, preprint, ([arXiv:1607.03150](https://arxiv.org/abs/1607.03150))
- Bhattacharya S., Kosowsky A., 2007, *ApJ*, **659**, L83
- Bhattacharya S., Kosowsky A., 2008, *Phys. Rev. D*, **77**, 083004
- Bianchi D., Gil-Marín H., Ruggeri R., Percival W. J., 2015, *MNRAS*, **453**, L11
- Blake C., et al., 2011, *MNRAS*, **415**, 2876
- Bobin J., Starck J.-L., Sureau F., Basak S., 2013, *A&A*, **550**, A73
- Bobin J., Sureau F., Starck J.-L., Rassat A., Paykari P., 2014, *A&A*, **563**, A105
- Bobin J., Sureau F., Starck J. L., 2016, *Astron. Astrophys.*, **591**, A50
- Bolton A. S., et al., 2012, *AJ*, **144**, 144
- Bregman J. N., 2007, *ARA&A*, **45**, 221
- Bundy K., et al., 2015, *ApJS*, **221**, 15
- Calabrese E., et al., 2014, *JCAP*, **1408**, 010
- Carlson J., Reid B., White M., 2013, *MNRAS*, **429**, 1674
- Carrasco J. J. M., Hertzberg M. P., Senatore L., 2012, *Journal of High Energy Physics*, **9**, 82
- Cavaliere A., Fusco-Femiano R., 1976, *A&A*, **49**, 137
- Cen R., Ostriker J. P., 1999, *ApJ*, **514**, 1
- Cen R., Ostriker J. P., 2006, *ApJ*, **650**, 560
- DESI Collaboration et al., 2016, preprint, ([arXiv:1611.00036](https://arxiv.org/abs/1611.00036))
- Dark Energy Survey Collaboration et al., 2016, *MNRAS*, **460**, 1270
- Davé R., Hernquist L., Katz N., Weinberg D. H., 1999, *ApJ*, **511**, 521
- Davis M., Peebles P. J. E., 1977, *ApJS*, **34**, 425
- Dawson K. S., et al., 2013, *AJ*, **145**, 10
- De Bernardis F., et al., 2016, preprint, ([arXiv:1607.02139](https://arxiv.org/abs/1607.02139))
- DeDeo S., Spergel D. N., Trac H., 2005, *ArXiv Astrophysics e-prints*,
- Doi M., et al., 2010, *AJ*, **139**, 1628
- Efron B., 1979, *Annals of Statistics*, **7**, 1
- Eisenstein D. J., et al., 2011, *AJ*, **142**, 72
- Feldman H. A., Kaiser N., Peacock J. A., 1994, *ApJ*, **426**, 23
- Ferraro S., Hill J. C., Battaglia N., Liu J., Spergel D. N., 2016, *Phys. Rev.*, **D94**, 123526
- Ferreira P. G., Juskiewicz R., Feldman H. A., Davis M., Jaffe A. H., 1999, *ApJ*, **515**, L1
- Flender S., Nagai D., McDonald M., 2016a, preprint, ([arXiv:1610.08029](https://arxiv.org/abs/1610.08029))
- Flender S., Bleem L., Finkel H., Habib S., Heitmann K., Holder G., 2016b, *ApJ*, **823**, 98
- Fukugita M., Peebles P. J. E., 2004, *ApJ*, **616**, 643
- Fukugita M., Ichikawa T., Gunn J. E., Doi M., Shimasaku K., Schneider D. P., 1996, *AJ*, **111**, 1748
- Fukugita M., Hogan C. J., Peebles P. J. E., 1998, *ApJ*, **503**, 518
- George E. M., et al., 2015, *ApJ*, **799**, 177
- Gil-Marín H., et al., 2016, *MNRAS*, **460**, 4188
- Górski K. M., Hivon E., Banday A. J., Wandelt B. D., Hansen F. K., Reinecke M., Bartelmann M., 2005, *ApJ*, **622**, 759
- Gunn J. E., et al., 1998, *AJ*, **116**, 3040
- Gunn J. E., et al., 2006, *AJ*, **131**, 2332
- Hand N., et al., 2012, *Physical Review Letters*, **109**, 041101
- Hartlap J., Simon P., Schneider P., 2007, *A&A*, **464**, 399
- Henderson S. W., et al., 2016, *J. Low. Temp. Phys.*, **184**, 772
- Hernández-Monteagudo C., Ho S., 2009, *MNRAS*, **398**, 790
- Hernández-Monteagudo C., Sunyaev R. A., 2008, *A&A*, **490**, 25
- Hernández-Monteagudo C., Verde L., Jimenez R., Spergel D. N., 2006, *ApJ*, **643**, 598
- Hernández-Monteagudo C., Ma Y.-Z., Kitaura F. S., Wang W., Génova-Santos R., Macías-Pérez J., Herranz D., 2015, *Physical Review Letters*, **115**, 191301
- Hill J. C., Ferraro S., Battaglia N., Liu J., Spergel D. N., 2016, *Physical Review Letters*, **117**, 051301
- Hinshaw G., et al., 2013, *ApJS*, **208**, 19
- Ho S., Dedeo S., Spergel D., 2009, preprint, ([arXiv:0903.2845](https://arxiv.org/abs/0903.2845))
- Hockney R. W. E. J. W., 1981, *Computer Simulation Using Particles*
- Jing Y. P., 2005, *ApJ*, **620**, 559
- Kaiser N., 1987, *MNRAS*, **227**, 1
- Keisler R., Schmidt F., 2013, *ApJ*, **765**, L32
- Kosowsky A., Bhattacharya S., 2009, *Phys. Rev. D*, **80**, 062003
- Laureijs R., et al., 2011, preprint, ([arXiv:1110.3193](https://arxiv.org/abs/1110.3193))
- Leauthaud A., et al., 2016, *MNRAS*, **457**, 4021
- Lesgourgues J., 2011
- Levi M., et al., 2013, preprint, ([arXiv:1308.0847](https://arxiv.org/abs/1308.0847))
- Ma Y.-Z., Zhao G.-B., 2014, *Physics Letters B*, **735**, 402
- Matsubara T., 2008, *Phys. Rev. D*, **77**, 063530
- Mostek N., Coil A. L., Cooper M., Davis M., Newman J. A., Weiner B. J., 2013, *ApJ*, **767**, 89
- Mueller E.-M., de Bernardis F., Bean R., Niemack M. D., 2015a, *Phys. Rev. D*, **92**, 063501
- Mueller E.-M., de Bernardis F., Bean R., Niemack M. D., 2015b, *ApJ*, **808**, 47
- Naess S., et al., 2014, *J. Cosmology Astropart. Phys.*, **10**, 007
- Norberg P., Baugh C. M., Gaztañaga E., Croton D. J., 2009, *MNRAS*, **396**, 19
- Okumura T., Seljak U., Vlah Z., Desjacques V., 2014, *J. Cosmology Astropart. Phys.*, **5**, 003
- Ostriker J. P., Vishniac E. T., 1986, *ApJ*, **306**, L51
- Parejko J. K., et al., 2013, *MNRAS*, **429**, 98
- Park C., 2000, *MNRAS*, **319**, 573
- Peacock J. A., Nicholson D., 1991, *MNRAS*, **253**, 307
- Peebles P. J. E., 1976, *Ap&SS*, **45**, 3
- Peebles P. J. E., 1980, The large-scale structure of the universe
- Planck Collaboration Ade P. A. R., et al., 2016a, *A&A*, **586**, A140
- Planck Collaboration et al., 2016b, *A&A*, **594**, A1
- Planck Collaboration et al., 2016c, *A&A*, **594**, A13
- Polarski D., Gannouji R., 2008, *Physics Letters B*, **660**, 439
- Press W. H., Schechter P., 1974, *ApJ*, **187**, 425
- Quenouille G., 1956, *Biometrika*, **43**, 353
- Reid B., et al., 2016, *MNRAS*, **455**, 1553
- Ross A. J., et al., 2012, *MNRAS*, **424**, 564
- Saito S., 2017, in prep.
- Saito S., et al., 2016, *MNRAS*, **460**, 1457
- Samushia L., Branchini E., Percival W. J., 2015, *MNRAS*, **452**, 3704
- Schaan E., et al., 2016, *Phys. Rev. D*, **93**, 082002
- Scoccimarro R., 2004, *Phys. Rev. D*, **70**, 083007
- Scoccimarro R., 2015, *Phys. Rev. D*, **92**, 083532
- Sefusatti E., Crocce M., Scoccimarro R., Couchman H. M. P., 2016, *MNRAS*, **460**, 3624
- Seljak U., McDonald P., 2011, *J. Cosmology Astropart. Phys.*, **11**, 039
- Shao J., Zhang P., Lin W., Jing Y., Pan J., 2011, *MNRAS*, **413**, 628

- Sheth R. K., Tormen G., 1999, *MNRAS*, **308**, 119
 Smith J. A., et al., 2002, *AJ*, **123**, 2121
 Soergel B., et al., 2016, *MNRAS*, **461**, 3172
 Spergel D., et al., 2013, preprint, ([arXiv:1305.5425](#))
 Steigman G., 2007, *Annual Review of Nuclear and Particle Science*, **57**, 463
 Sugiyama N. S., 2014, *ApJ*, **788**, 63
 Sugiyama N. S., Okumura T., Spergel D. N., 2016a, preprint, ([arXiv:1606.06367](#))
 Sugiyama N. S., Okumura T., Spergel D. N., 2016b, *JCAP*, **1607**, 001
 Sunyaev R. A., Zeldovich Y. B., 1970, *Ap&SS*, **7**, 3
 Sunyaev R. A., Zeldovich Y. B., 1972, *Comments on Astrophysics and Space Physics*, **4**, 173
 Sunyaev R. A., Zeldovich I. B., 1980, *MNRAS*, **190**, 413
 Swetz D. S., et al., 2011, *ApJS*, **194**, 41
 Takada M., et al., 2014, *PASJ*, **66**, R1
 Taruya A., Nishimichi T., Saito S., 2010, *Phys. Rev. D*, **82**, 063522
 Tegmark M., Taylor A. N., Heavens A. F., 1997, *ApJ*, **480**, 22
 The Dark Energy Survey Collaboration 2005, *ArXiv Astrophysics e-prints*,
 Tukey J. W., 1958, *Ann. Math. Stat.*, **29**, 614
 White M., et al., 2011, *ApJ*, **728**, 126
 Wilson M. J., Peacock J. A., Taylor A. N., de la Torre S., 2015, preprint, ([arXiv:1511.07799](#))
 Wright E. L., et al., 2010, *AJ*, **140**, 1868
 Yamamoto K., Nakamichi M., Kamino A., Bassett B. A., Nishioka H., 2006, *PASJ*, **58**, 93
 Yoo J., Seljak U., 2015, *MNRAS*, **447**, 1789

APPENDIX A: COVARIANCE MATRICES

While there are a few analytic approaches for the covariance of pairwise velocities (Bhattacharya & Kosowsky 2008; Mueller et al. 2015b), they do not include contamination of the kSZ signal, e.g. primary CMB anisotropies and detector noise. In Sugiyama et al. (2016a), we have presented the model of the covariance of the pairwise kSZ power multipoles, which may include the contamination. In this appendix, to validate our covariance model, we compare our model with covariance estimates from data itself using the jackknife (JK) (Quenouille 1956; Tukey 1958) and bootstrap (BS) (Efron 1979) methods. Section A1 presents the model of the covariance in linear theory, and Section A2 compares the model with the measurement from the data.

A1 Theory

We estimate the CMB temperature distortion associated with each galaxy by applying the AP filter (Sec. 3.1). Then, we model the observed CMB temperature in the AP filtered CMB map as follows

$$\delta T_{\text{AP}}(\hat{n}_i; \theta_c) = \delta T_{\text{kSZ}}^{(\text{AP})}(\hat{n}_i; \theta_c) + \delta T_{\text{N}}^{(\text{AP})}(\hat{n}_i; \theta_c), \quad (\text{A1})$$

where θ_c denotes the AP filter radius, the line-of-sight \hat{n}_i points to galaxy i from the observer, $\delta T_{\text{kSZ}}^{(\text{AP})} = -(T_0 \tau / c) \vec{v} \cdot \hat{n}$ (equation 15) represents the kSZ signal, and $\delta T_{\text{N}}^{(\text{AP})}$ is the total noise on the kSZ signal, which may include primary CMB anisotropies, detector noise, thermal SZ effect, and residual foregrounds. Since we measure the CMB temperature distortion subtracting its average (equation 42),

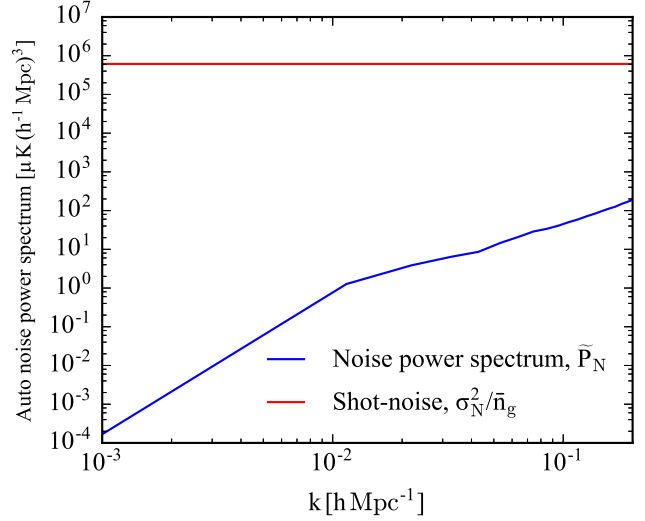


Figure A1. Auto power spectrum of the noise fluctuation \tilde{P}_{N} (blue line) and its shot-noise term $\sigma_{\text{N}}^2/\bar{n}_{\text{g}}$ (red line) in the AP filtered WPR2 map (Sec. 2.1). The AP filtered \tilde{P}_{N} is about 10^3 times smaller than the shot-noise $\sigma_{\text{N}}^2/\bar{n}_{\text{g}}$ at the scales of interest ($k < 0.2 \text{ h Mpc}^{-1}$); therefore, we can make an approximation that the AP filtered noise fluctuation $\delta T_{\text{N}}^{(\text{AP})}$ is an uncorrelated, Gaussian field (equation A4) on large scales.

the ensemble averages of $\delta T_{\text{kSZ}}^{(\text{AP})}$ and $\delta T_{\text{N}}^{(\text{AP})}$ will be zero: $\langle \delta T_{\text{kSZ}}^{(\text{AP})} \rangle = \langle \delta T_{\text{N}}^{(\text{AP})} \rangle = 0$.

The pairwise kSZ power spectrum (equation 25) including the noise $\delta T_{\text{N}}^{(\text{AP})}$ for aperture radius θ_c is given by

$$P_{\text{kSZ}}(\vec{k}; \theta_c) = \left\langle -\frac{V}{N^2} \sum_{i,j} [\delta T_{\text{kSZ}}^{(\text{AP})}(\hat{n}_i; \theta_c) - \delta T_{\text{kSZ}}^{(\text{AP})}(\hat{n}_j; \theta_c)] e^{-i\vec{k} \cdot (\vec{s}_i - \vec{s}_j)} \right\rangle + \left\langle -\frac{V}{N^2} \sum_{i,j} [\delta T_{\text{N}}^{(\text{AP})}(\hat{n}_i; \theta_c) - \delta T_{\text{N}}^{(\text{AP})}(\hat{n}_j; \theta_c)] e^{-i\vec{k} \cdot (\vec{s}_i - \vec{s}_j)} \right\rangle, \quad (\text{A2})$$

where \vec{s}_i denotes the observed coordinates of galaxy i , N represents the total number of observed galaxies, and V is survey volume. In the pairwise kSZ signal, the contribution from the noise in the second line of equation (A2) becomes zero, because its parity is even, while the parity of the kSZ signal is odd (Sec. 4.2).

The kSZ power covariance can be formally expressed in terms of Gaussian (unconnected) and non-Gaussian (connected) contributions in cumulant expansion. The Gaussian term has only diagonal elements of the covariance matrix, and the power spectrum estimates of different scales are uncorrelated, while non-vanishing off-diagonal elements arise from the non-Gaussian term on small scales. Linear theory only yields the Gaussian term, described as

$$\text{Cov}(\hat{P}_{\text{kSZ}, \ell=1}(k_1; \theta_a), \hat{P}_{\text{kSZ}, \ell=1}^*(k_2; \theta_b)) = \frac{\delta_{k_1 k_2}^{\text{K}}}{N_{\text{mode}}(k_1)} C_{\text{kSZ}}(k_1; \theta_a, \theta_b), \quad (\text{A3})$$

where $\hat{P}_{\text{kSZ}, \ell=1}(k; \theta)$ is the pairwise kSZ power dipole estimated for aperture radius θ (equation 44), $N_{\text{mode}} = 4\pi k^2 \Delta k V / (2\pi)^3$ is the number of independent Fourier modes in a bin, Δk is the bin width, and δ^{K} denotes the Kronecker delta such that $\delta_{k_1 k_2}^{\text{K}} = 1$ if $k_1 = k_2$ within the bin width, otherwise zero.

Since the AP filtering removes most of any large-scale noise contributions, we assume that the AP filtered noise fluctuation $\delta T_{\text{N}}^{(\text{AP})}$ is an uncorrelated, Gaussian field that

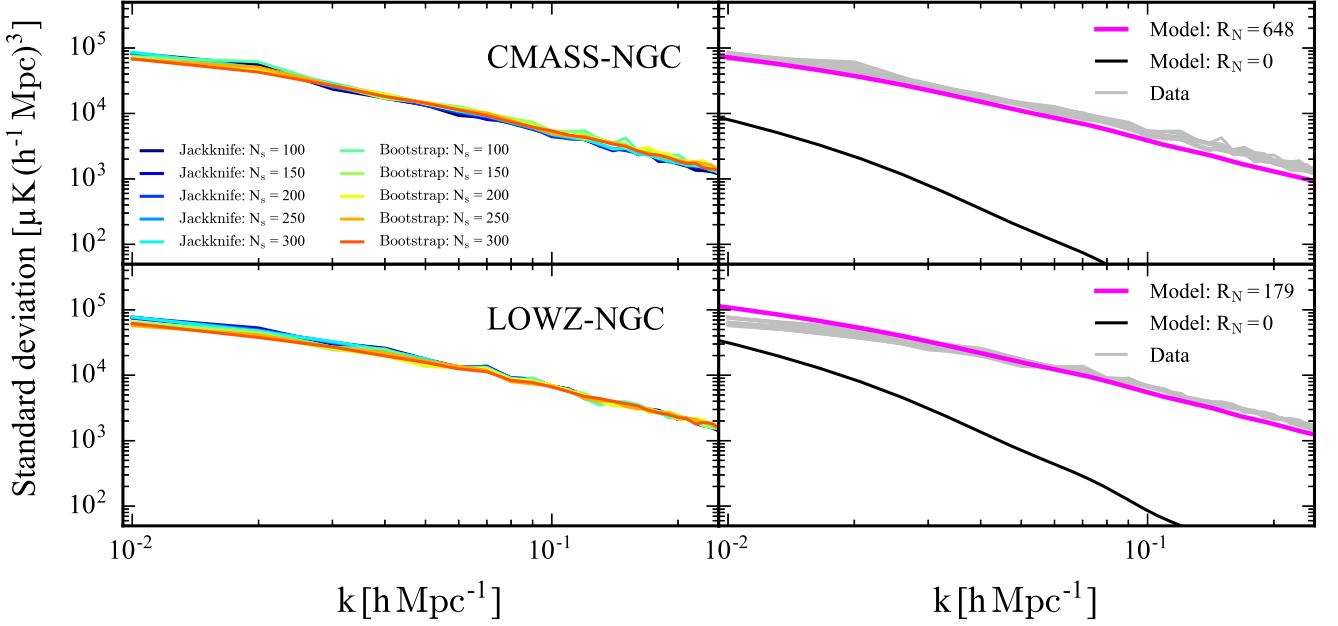


Figure A2. Left: Standard deviations of the pairwise kSZ power dipole as a function of scales for different internal error estimates using the jackknife and bootstrap methods for various spatial sub-regions on the sky ($N_s = 100, 150, 200, 250,$ and 300). Data used here are the WPR2 map for $5'$ aperture with the LOWZ-NGC (left bottom panel) and CMASS-NGC (left top panel) samples. Right: Comparisons of the internal error estimates with the predictions from our model in equation (A8). The grey lines are the same as the coloured lines in the left panel. The black and magenta solid lines show the linear theory predictions for a noise less sky map ($R_N = 0$) and the WPR2 map ($R_N = 179$ for LOWZ and $R_N = 648$ for CMASS), respectively. The values of the inverse signal-to-noise ratio R_N are estimated using the WPR2 map and the linear theory predictions of the LOS velocity dispersion (see text for further details). Our model is consistent with the internal error estimates, which means that the AP filtered noise properties on the kSZ signal can be explained by an uncorrelated, Gaussian field (equation A4).

satisfies

$$\langle \delta T_N^{(\text{AP})}(\hat{n}_i; \theta_a) \delta T_N^{(\text{AP})}(\hat{n}_j; \theta_b) \rangle_c = \sigma_N^2(\theta_a, \theta_b) \delta_{ij}, \quad (\text{A4})$$

where $\langle \dots \rangle_c$ denotes a cumulant. In the above expression, the root-mean-square (rms) of the noise fluctuation, σ_N , is given by

$$\sigma_N^2(\theta_a, \theta_b) = \sum_{\ell} \frac{2\ell + 1}{4\pi} C_{\ell} U(\ell\theta_a) U(\ell\theta_b), \quad (\text{A5})$$

where C_{ℓ} is the CMB angular power spectrum, and U_{ℓ} is the AP filter function (equation 11). On the other hand, the rms of the kSZ signal, which represents a typical kSZ temperature, is given by

$$\sigma_{\text{kSZ}}(\theta_c) = \left(\frac{T_0 \tau(\theta_c)}{c} \right) \sigma_v, \quad (\text{A6})$$

where the optical depth $\tau(\theta_c)$ as a function of aperture radii is given by equation (17), and σ_v is the LOS velocity dispersion, which is computed by $\sigma_v = (aHf\sigma_8)\sigma_0$ with $\sigma_0^2 = \frac{1}{3} \int \frac{dk}{2\pi^2} P_{\text{lin}}(k)$ in linear theory. Then, to estimate the impact of the noise level, we define the following inverse signal-to-noise ratio as

$$R_N^2(\theta_a, \theta_b) = \frac{\sigma_N^2(\theta_a, \theta_b)}{\sigma_{\text{kSZ}}(\theta_a) \sigma_{\text{kSZ}}(\theta_b)}. \quad (\text{A7})$$

Under the assumption in equation (A4), we finally calculate C_{kSZ} in linear theory (see equation (4.9) in Sugiyama et al.

(2016a)):

$$\begin{aligned} C_{\text{kSZ}}(k; \theta_a, \theta_b) &= 18 \left(\frac{T_0 H_0}{c} \right)^2 a^2 E^2 \tau(\theta_a) \tau(\theta_b) (f\sigma_8)^2 \\ &\left[\left(\frac{4}{5} (b\sigma_8)^2 + \frac{8}{7} (b\sigma_8)(f\sigma_8) + \frac{4}{9} (f\sigma_8)^2 \right) \frac{(P_{\text{lin}}(k))^2}{k^2} \right. \\ &+ \frac{\sigma_0^2}{\bar{n}_g} (1 + R_N^2(\theta_a, \theta_b)) \left(\frac{2}{3} (b\sigma_8)^2 + \frac{4}{5} (b\sigma_8)(f\sigma_8) + \frac{2}{7} (f\sigma_8)^2 \right) P_{\text{lin}}(k) \\ &\left. + \frac{2}{5} \frac{1}{\bar{n}_g} \frac{P_{\text{lin}}(k)}{k^2} + \frac{2}{3} \frac{\sigma_0^2}{\bar{n}_g^2} (1 + R_N^2(\theta_a, \theta_b)) \right], \quad (\text{A8}) \end{aligned}$$

where \bar{n}_g is the galaxy mean number density. The above expression holds true even if $\langle \delta T_N^{(\text{AP})} \rangle \neq 0$ as shown in Sugiyama et al. (2016a).

To validate the assumption of the noise property in equation (A4), we calculate the auto power spectrum of the noise fluctuation δT_N , which mainly contributes to the covariance of the pairwise kSZ dipole, without the assumption. In linear theory, we have

$$\begin{aligned} P_N(\vec{k}; \theta_a, \theta_b) &= \frac{V}{N^2} \sum_{i,j} \langle \delta T_N^{(\text{AP})}(\hat{n}_i; \theta_a) T_N^{(\text{AP})}(\hat{n}_j; \theta_b) \rangle_c e^{-i\vec{k} \cdot (\vec{s}_i - \vec{s}_j)}, \\ &= \tilde{P}_N(\vec{k}; \theta_a, \theta_b) + \frac{\sigma_N^2(\theta_a, \theta_b)}{\bar{n}_g}, \quad (\text{A9}) \end{aligned}$$

where \tilde{P}_N is given by

$$\tilde{P}_N(\vec{k}; \theta_a, \theta_b) = \frac{1}{V} \sum_{\ell m} C_\ell U(\ell\theta_a) U(\ell\theta_b) Y_\ell^m(\hat{k}) Y_\ell^{m*}(\hat{k}) \left[4\pi \int_0^{x_{\max}} dx x^2 j_\ell(kx) \right]^2, \quad (\text{A10})$$

and the shot-noise term σ_N^2/\bar{n}_g appears in our covariance model in equation (A8). Since the assumption in equation (A4) only yields the shot-noise term, we show that \tilde{P}_N is small enough to be ignored compared to σ_N^2/\bar{n}_g . Fig. A1 shows \tilde{P}_N (blue line) and σ_N^2/\bar{n}_g (red line) for $\theta_a = \theta_b = 5'$, $\bar{n}_g = 3.0 \times 10^{-4} h^3 \text{Mpc}^{-3}$, and $V = (4\pi/3)x_{\max}^3 = 1 h^{-1} \text{Gpc}$. The CMB angular power spectrum C_ℓ is computed from the WPR2 map we use in this work (Sec. 2.1), which includes all of the noise components. As expected, we find that the shot-noise term σ_N^2/\bar{n}_g is dominant, and the AP filtered noise power spectrum \tilde{P}_N is about 10^3 times smaller than the shot noise at the scales of interest ($k < 0.2 h \text{Mpc}^{-1}$).

A2 Comparisons with data

We estimate the data covariance matrices through the resampling of data itself, using jackknife (Quenouille 1956; Tukey 1958) and bootstrap (Efron 1979) methods. The galaxy dataset has been split into N_s spatial sub-regions on the sky. For the jackknife method, a copy of data is defined by systematically omitting, in turn, each of N_s sub-regions. For the bootstrap method, N_s sub-regions are selected at random with replacement from the initial data set.

In the jackknife and bootstrap schemes, the covariance matrices are estimated by

$$C_{\text{JK},ij} = \frac{N_s - 1}{N_s} \sum_k \left(y_i^k - \bar{y}_i \right) \left(y_j^k - \bar{y}_j \right)$$

$$C_{\text{BS},ij} = \frac{1}{N_s - 1} \sum_k \left(y_i^k - \bar{y}_i \right) \left(y_j^k - \bar{y}_j \right), \quad (\text{A11})$$

where y_i^k is the i th measure of the statistic of interest for the k th configuration, and $\bar{y}_i = \frac{1}{N_s} \sum_k y_i^k$. Here, we choose $y_i = P_{\text{kSZ},\ell=1}(k_i)$.

We calculate the rms noise $\sigma_N(\theta_c) = \sqrt{\sigma_N^2(\theta_c, \theta_c)}$ in equation (A5) from the WPR2 map for $5'$ aperture; we find $\sigma_N = 13.6 \mu K$. In linear theory, the LOS velocity dispersion is $\sigma_v = 253 \text{ km s}^{-1}$ for LOWZ and $\sigma_v = 281 \text{ km s}^{-1}$ for CMASS, which correspond to typical kSZ temperatures of $\sigma_{\text{kSZ}} = 0.076 \mu K$ and $\sigma_{\text{kSZ}} = 0.021 \mu K$, respectively, where we used the best fit values of the optical depth τE for $5'$ aperture in Table 1. As a result, we evaluate inverse signal-to-noise ratios of $R_N = 179$ for LOWZ and $R_N = 648$ for CMASS.

The left panels of Fig. A2 show the standard deviations of the pairwise kSZ power dipole for different internal error estimates using the jackknife and bootstrap methods for various spatial sub-regions on the sky (coloured lines). We use the WPR2 map for $5'$ aperture with the LOWZ-NGC (left bottom panel) and CMASS-NGC (left top panel) samples. In the right panels, we compare the internal error estimates (grey lines) with the predictions from our model in equation (A8), where we use $\bar{n}_g = 3.6 (2.6) \times 10^{-4} (h^{-1} \text{Mpc})^{-3}$,

$V = 0.90 (2.57) (h^{-1} \text{Gpc})^3$, and $R_N = 179 (648)$ for the LOWZ-NGC (CMASS-NGC) sample. The grey lines in the right panels are the same as the coloured lines in the left panels, and the black and magenta solid lines are the linear theory predictions for a noise less sky map ($R_N = 0$) and the WPR2 map ($R_N = 179$ for LOWZ and $R_N = 648$ for CMASS), respectively. We can find an excellent agreement between the covariance estimates from the model and the data, indicating that the property of the AP filtered noise on the kSZ signal can be explained as an uncorrelated, Gaussian field (equation A4).

APPENDIX B: DETAILS OF HOW TO MEASURE THE PAIRWISE KSZ POWER SPECTRUM

In this appendix, we detail how to measure the pairwise kSZ power spectrum from galaxy catalogues.

B1 Estimator

We start with rewriting equation (44):

$$\hat{P}_{\text{kSZ},\ell}(\vec{k}) = -\frac{(2\ell+1)}{A} \int d^3 s_1 \int d^3 s_2 e^{-i\vec{k}\cdot\vec{s}_{12}} \mathcal{L}_\ell(\hat{k} \cdot \hat{n}_{12}) \times \left[\delta T(\vec{s}_1) \delta n(\vec{s}_2) - \delta n(\vec{s}_1) \delta T(\vec{s}_2) \right]. \quad (\text{B1})$$

As the integrals over \vec{s}_1 and \vec{s}_2 in the above expression are not separable due to the \hat{n}_{12} dependence in $\mathcal{L}_{\ell \geq 1}(\hat{k} \cdot \hat{n}_{12})$, the computation of the estimator will be $\mathcal{O}(N_k \times N^2)$, where N_k and N are the numbers of k -modes and observed galaxies, respectively. Since the estimator is computationally challenging, we provide a fast method to measure the pairwise kSZ power multipoles using the local plane parallel approximation,

$$\mathcal{L}_\ell(\hat{k} \cdot \hat{n}_{12}) \approx \mathcal{L}_\ell(\hat{k} \cdot \hat{s}_1) \approx \mathcal{L}_\ell(\hat{k} \cdot \hat{s}_2). \quad (\text{B2})$$

This approximation allows the integrals in equation (44) to decouple into a product of Fourier transforms (Yamamoto et al. 2006; Blake et al. 2011; Beutler et al. 2014; Samushia et al. 2015), which reduces the process to $\mathcal{O}(N_k \times N)$:

$$\hat{P}_{\text{kSZ},\ell}(\vec{k}) = -\frac{(2\ell+1)}{A} \left[\delta T_\ell(\vec{k}) \delta n_\ell^*(\vec{k}) - \text{c.c.} \right], \quad (\text{B3})$$

where $\delta n(\vec{k})$ is the Fourier transform of the density fluctuation $\delta n(\vec{s})$:

$$\delta n(\vec{k}) = \int d^3 s e^{-i\vec{k}\cdot\vec{s}} \delta n(\vec{s}), \quad (\text{B4})$$

and $\delta T_\ell(\vec{k})$ is the multipole component of the kSZ temperature fluctuation $\delta T(\vec{s})$, given by

$$\delta T_\ell(\vec{k}) = \int d^3 s e^{-i\vec{k}\cdot\vec{s}} \mathcal{L}_\ell(\hat{k} \cdot \hat{s}) \delta T(\vec{s}). \quad (\text{B5})$$

This approximation has been known to be accurate on the scales of interest for the galaxy power spectrum ($k \lesssim 0.2 h \text{Mpc}^{-1}$) (Samushia et al. 2015; Yoo & Seljak 2015), and we expect that it can be also applied to the pairwise kSZ power spectrum. Furthermore, as pointed out in (Bianchi et al. 2015; Scoccimarro 2015), $\delta T_\ell(\vec{k})$ can be built to be computable using any fast Fourier transform (FFT)

algorithm, leading to $\mathcal{O}(N_k \log N_k)$: e.g. for $\ell = 1$ and $\ell = 3$, we have

$$\begin{aligned}\delta T_{\ell=1}(\vec{k}) &= \hat{k}_i \delta T_i(\vec{k}), \\ \delta T_{\ell=3}(\vec{k}) &= \frac{5}{2} \hat{k}_i \hat{k}_j \hat{k}_k \delta T_{ijk}(\vec{k}) - \frac{3}{2} \hat{k}_i \delta T_i(\vec{k}),\end{aligned}\quad (\text{B6})$$

with

$$\delta T_{i_1 \dots i_n}(\vec{k}) = \int d^3 s e^{-i\vec{k} \cdot \vec{s}} \hat{s}_{i_1} \dots \hat{s}_{i_n} \delta T(\vec{s}), \quad (\text{B7})$$

where we follow the convention that summation is implied for repeated indices. By symmetry, δT_i and δT_{ijk} can be computed by 3 and 10 FFTs, respectively.

B2 Prescription of FFT

The FFT algorithm requires the interpolation of functions on a regular grid in position space. For any function $F(\vec{s})$, the interpolation over the grid can be mathematically described in terms of the mass assignment function $W_{\text{mass}}(\vec{s})$ and the sampling function $\Pi(\vec{s})$ as follows

$$\tilde{F}_1(\vec{s}) = \Pi(\vec{s}) \int d^3 s' W_{\text{mass}}(\vec{s} - \vec{s}') F(\vec{s}'). \quad (\text{B8})$$

In the above expression, the sampling function is defined as

$$\Pi(\vec{s}) = G^3 \sum_{\vec{n}} \delta_{\text{D}}(\vec{s} - \vec{G}), \quad (\text{B9})$$

where $\vec{G} = \{G_x n_x, G_y n_y, G_z n_z\}$ denotes grid points, \vec{n} is an integer vector, $G_{i=x,y,z}$ are the grid spacing, $G^3 \equiv G_x G_y G_z$, and the summation is over all three-dimensional integer vectors. The Fourier transform of $\tilde{F}_1(\vec{s})$ is given by

$$\begin{aligned}\tilde{F}_1(\vec{k}) &= \int_V d^3 s e^{-i\vec{k} \cdot \vec{s}} \tilde{F}_1(\vec{s}) \\ &= \sum_{\vec{n}} W_{\text{mass}}(\vec{k} - \vec{k}_{\text{f}}) F(\vec{k} - \vec{k}_{\text{f}}),\end{aligned}\quad (\text{B10})$$

where $\vec{k}_{\text{f}} = (2\pi)\{n_x/G_x, n_y/G_y, n_z/G_z\}$, and $W_{\text{mass}}(\vec{k})$ and $F(\vec{k})$ are the Fourier transforms of $W_{\text{mass}}(\vec{s})$ and $F(\vec{s})$, respectively. Thus, the finite sampling results in the ‘‘alias’’ sums: i.e., the sums over \vec{n} (Jing 2005).

To reduce the aliasing contribution, we adopt a simple technique proposed by (Hockney R. W. 1981; Sefusatti et al. 2016) that is based on the interlacing of two grids. The method significantly reduces the aliasing effect. Sefusatti et al. (2016) has not shown corrections for the shot-noise term, but the shot-noise term does not appear in the pairwise kSZ power multipoles (equation 44); therefore, we can apply this method to our kSZ analysis directly. We first prepare $\tilde{F}_1(\vec{k})$ obtained by equation (B10). Second, we perform the interpolation on a grid shifted by the distance $\vec{G}/2$

$$\begin{aligned}\tilde{F}_2(\vec{k}) &= \int_V d^3 s e^{-i\vec{k} \cdot \vec{s}} \Pi\left(\vec{s} + \frac{\vec{G}}{2}\right) \int d^3 s' W_{\text{mass}}(\vec{s} - \vec{s}') F(\vec{s}') \\ &= \sum_{\vec{n}} (-1)^{n_{xyz}} W_{\text{mass}}(\vec{k} - \vec{k}_{\text{f}}) F(\vec{k} - \vec{k}_{\text{f}}),\end{aligned}\quad (\text{B11})$$

where $n_{xyz} = n_x + n_y + n_z$. As a simple method to compute $\tilde{F}_2(\vec{k})$, we compute $F(\vec{s})$ for spatial galaxy positions shifted by the distance $\vec{G}/2$ (Saito 2017)

$$F'(\vec{s}) = F\left(\vec{s} - \frac{\vec{G}}{2}\right) = \sum_i^N F_i \delta_{\text{D}}\left(\vec{s} - \vec{s}_i - \frac{\vec{G}}{2}\right), \quad (\text{B12})$$

where $F(\vec{s}) = \sum_i^N F_i \delta_{\text{D}}(\vec{s} - \vec{s}_i)$ with F_i being a weight at galaxy i . Then, we can show that the Fourier transform of $F'(\vec{s})$ in equation (B10) is related to $\tilde{F}_2(\vec{k})$ through

$$\tilde{F}_2(\vec{k}) = e^{\frac{i}{2} \vec{k} \cdot \vec{G}} \tilde{F}'_1(\vec{k}). \quad (\text{B13})$$

Finally, we derive

$$\begin{aligned}\tilde{F}(\vec{k}) &= \frac{1}{2} \left(\tilde{F}'_1(\vec{k}) + \tilde{F}_2(\vec{k}) \right) \\ &= \frac{1}{2} \sum_{\vec{n}} (1 + (-1)^{n_{xyz}}) W_{\text{mass}}(\vec{k} - \vec{k}_{\text{f}}) F(\vec{k} - \vec{k}_{\text{f}}).\end{aligned}\quad (\text{B14})$$

Thus, all the aliasing contributions correspond to odd values of the sum $n_x + n_y + n_z$, and can be partially corrected. In particular, the largest contributions for $|\vec{n}| = 1$ are removed.

The Fourier transform of a function $F(\vec{s})$ measured by FFT, $F(\vec{k})|_{\text{FFT}}$, includes the effect of the mass assignment function $W_{\text{mass}}(\vec{k})$ (Jing 2005). We can remove such effects from $F(\vec{k})|_{\text{FFT}}$ by simply dividing by $W_{\text{mass}}(\vec{k})$: $F(\vec{k}) = F(\vec{k})|_{\text{FFT}} / W_{\text{mass}}(\vec{k})$. The most popular mass assignment function is given by

$$W_{\text{mass}}(\vec{k}) = \prod_{i=x,y,z} \left[\text{sinc} \left(\frac{\pi k_i}{2k_{\text{N},i}} \right) \right]^p, \quad (\text{B15})$$

where $k_{\text{N},i} = \pi/H_i$ is the Nyquist frequency of i -axis with the grid spacing H_i on the axis. The indexes $p = 1$, $p = 2$, and $p = 3$ correspond to the nearest grid point (NGP), cloud-in-cell (CIC), and triangular-shaped cloud (TSC) assignment functions, respectively.

APPENDIX C: DERIVATION OF EQUATION (53)

A Hankel transform relates the pairwise kSZ power spectrum estimator averaged in spherical shell of \vec{k} (equations 44 and 50) to the pairwise kSZ correlation function estimator normalized by the constant factor A (equation 45):

$$\hat{P}_{\text{kSZ}, \ell}(k) = 4\pi(-i)^\ell \int ds s^2 j_\ell(ks) \hat{\xi}_{\text{kSZ}, \ell}(s) \quad (\text{C1})$$

where

$$\begin{aligned}\hat{\xi}_{\text{kSZ}, \ell}(s) &= -\frac{(2\ell+1)}{A} \int \frac{d\Omega_s}{4\pi} \int d^3 s_1 \int d^3 s_2 \delta_{\text{D}}(\vec{s} - \vec{s}_{12}) \\ &\quad \times \mathcal{L}_\ell(\hat{s}_{12} \cdot \hat{n}_{12}) \left[\delta T(\vec{s}_1) \delta n(\vec{s}_2) - \delta n(\vec{s}_1) \delta T(\vec{s}_2) \right].\end{aligned}\quad (\text{C2})$$

A way to construct a theoretical model to explain what we observe, $\hat{P}_{\text{kSZ}, \ell}(k)$ (equation 44), is to compute its ensemble average, $\langle \hat{P}_{\text{kSZ}, \ell}(k) \rangle$, which may include survey geometry effects. The observed galaxy and kSZ fields, respectively δn and δT , are multiplied by a mask that accounts for both the survey geometry and the completeness weight (equation 1). The ensemble average of the square bracket in equation (C2) is given by

$$\begin{aligned}&\langle \delta T(\vec{s}_1) \delta n(\vec{s}_2) - \delta n(\vec{s}_1) \delta T(\vec{s}_2) \rangle \\ &= -\bar{n}(\vec{s}_1) \bar{n}(\vec{s}_2) \sum_{\ell} \xi_{\text{kSZ}, \ell}(|\vec{s}_{12}|) \mathcal{L}_\ell(\hat{s}_{12} \cdot \hat{n}_{12}),\end{aligned}\quad (\text{C3})$$

where the number density computed from a random catalogue $\bar{n}(\vec{s}_1)$ given by equation (46) corresponds to the survey mask. Using the relation,

$$\mathcal{L}_\ell(\mu) \mathcal{L}_{\ell_1}(\mu) = \sum_{\ell_2} (2\ell_2 + 1) \begin{pmatrix} \ell & \ell_1 & \ell_2 \\ 0 & 0 & 0 \end{pmatrix}^2 \mathcal{L}_{\ell_2}(\mu), \quad (\text{C4})$$

we derive

$$\langle \widehat{\xi}_{\text{kSZ}, \ell}(s) \rangle = (2\ell + 1) \sum_{\ell_1 \ell_2} \begin{pmatrix} \ell & \ell_1 & \ell_2 \\ 0 & 0 & 0 \end{pmatrix}^2 \xi_{\text{kSZ}, \ell_1}(s) Q_{\ell_2}(s), \quad (\text{C5})$$

where $\begin{pmatrix} \ell_1 & \ell_2 & \ell \\ m_1 & m_2 & m \end{pmatrix}$ is the Wigner 3j symbol, and the survey window function multipoles $Q_\ell(s)$ are given by

$$Q_\ell(s) = \frac{(2\ell + 1)}{A} \int \frac{d\Omega_s}{4\pi} \int d^3 s_1 \int d^3 s_2 \delta_{\text{D}}(\vec{s} - \vec{s}_{12}) \times \mathcal{L}_\ell(\hat{s}_{12} \cdot \hat{n}_{12}) \bar{n}(\vec{s}_1) \bar{n}(\vec{s}_2). \quad (\text{C6})$$

In the local plane parallel approximation, $\hat{n}_{12} \sim \hat{s}_1$, we have

$$Q_\ell(s) = \frac{(2\ell + 1)}{A} \int \frac{d\Omega_s}{4\pi} \int \frac{d^3 k}{(2\pi)^3} e^{i\vec{k} \cdot \vec{s}} \bar{n}_\ell(\vec{k}) \bar{n}^*(\vec{k}), \quad (\text{C7})$$

where $\bar{n}(\vec{k})$ is the Fourier transform of $\bar{n}(\vec{s})$, and $\bar{n}_\ell(\vec{k})$ can be obtained by

$$\begin{aligned} \bar{n}(\vec{k}) &= \int d^3 s e^{-i\vec{k} \cdot \vec{s}} \bar{n}(\vec{s}) \\ \bar{n}_\ell(\vec{k}) &= \int d^3 s e^{-i\vec{k} \cdot \vec{s}} \mathcal{L}_\ell(\hat{k} \cdot \hat{s}) \bar{n}(\vec{s}). \end{aligned} \quad (\text{C8})$$

Substituting equation (C5) into equation (C1) results in equation (53). In this work, we do not take into account the integral constant correction (Peacock & Nicholson 1991), because we expect that the effect would be a subdominant contribution to the corrections from the survey window function. We leave a more detailed discussion of the effect as future works.

This paper has been typeset from a $\text{\TeX}/\text{\LaTeX}$ file prepared by the author.